

Stability analysis of a Newtonian film flow over hydrophobic microtextured substrates

D. Pettas ¹, G. Karapetsas ², Y. Dimakopoulos ¹, and J. Tsamopoulos ^{1,*}

¹*Laboratory of Fluid Mechanics and Rheology, Department of Chemical, University of Patras, Patras 26500, Greece*

²*Department of Chemical Engineering, Aristotle University of Thessaloniki, Thessaloniki 54124, Greece*



(Received 31 July 2021; revised 8 January 2022; accepted 24 February 2022; published 21 March 2022)

We consider the flow of a Newtonian liquid film over an inclined hydrophobic wall textured with periodical microgrooves, the depth of which is much longer than their width, which is of the order of the capillary length of the liquid. Due to their structure, these grooves can be likened to slits. The flowing liquid fails to thoroughly wet the topography forming a second liquid-gas interface, with air encapsulated inside the topographical features. Under these conditions, two possible flow configurations may arise: (1) the inner interface will be pinned at the edges of the slit (ideal Cassie-Baxter state) and (2) the film may partially wet the sidewalls of the slits, forming two additional contact lines with the substrate. We investigate both the steady flow and the stability of a Newtonian liquid film flowing over various substrates with such flow configuration. We solve the 2D Navier-Stokes equations and develop a finite element model to accurately describe the exact shape of all liquid-gas interfaces at a steady state. We determine the linear stability of the steady-state solutions when subjected to perturbations in the streamwise direction and employ the Floquet-Bloch theory to account for disturbances of arbitrary wavelengths, i.e., not necessarily matching the periodicity of the substrate. Through numerical simulations, we highlight the effect of inertia, viscous and capillary forces, and the mobility of the contact line on the stability of the fluid flow. We examine the impact of substrate wettability and orientation with respect to gravity and geometric characteristics of the substrate. It is demonstrated that when the film partially wets the sidewalls of the trench, multiple steady states may arise, which are analyzed for their stability characteristics. It is also shown that the second air-liquid interface and the air pockets inside the grooves of a structured hydrophobic surface may considerably stabilize the flow mainly by the capillary forces, which act as a damper, preventing the disturbances of the outer free surface to grow.

DOI: [10.1103/PhysRevFluids.7.034004](https://doi.org/10.1103/PhysRevFluids.7.034004)

I. INTRODUCTION

Film flows have drawn considerable attention over the years due to the broad range of applications in various environmental and engineering applications [1]. Some prominent examples include coating applications [2], heat exchangers [3], as well as the development of smart materials such as self-cleaning and anti-icing surfaces [4–6]. Thin films are also related to the wettability and spreading of fluids over hydrophobic substrates [7]. In principle, the substrates encountered are frequently rough, either by design or due to their nature. In the former case, the substrates are often fabricated with well-defined ridges, pillars, or corrugations that protrude from a flat substrate.

*Corresponding author: tsamo@chemeng.upatras.gr

The size of the features ranges from a few nanometers to some microns. Due to the small scale of these topographical features, the liquid film may surpass the cavities of the substrate resulting in air encapsulation, which in turn may significantly affect the flow dynamics. As a result, when the liquid is flowing, it experiences an apparent slip due to the presence of the inner liquid-gas interface [8–10].

In the literature, the most widely studied case is when the film completely wets the solid structures. This flow configuration is the desired arrangement in many coating applications and is known as Wenzel state [11]. Several theoretical studies [12–14] and experimental works [13,14] have been devoted to describing film flow dynamics over thoroughly wetted textured walls. They concluded that the film deformation is mainly affected by the combined effect of the capillary and inertia forces of the film and the morphology of the substrate. Moreover, Wierschem *et al.* [15] and Nguyen and Bontozoglou [16] studied the flow of films over corrugated surfaces and focused on the transition from creeping flow to the inertia-dominated regime. It was demonstrated that for a specific range of flowrates, the film acquires a highly distorted shape due to the resonance between the deformable liquid-air interface and the substrate topography, resulting in the appearance of standing waves.

As mentioned above, though, the Wenzel wetting state cannot always be achieved since air may become entrapped inside the topographical features during the coating process [9]. The presence of gas pockets inside these structures leads to limited contact between the liquid and the solid surface, enhancing the mobility of the fluid; this wetting state is known in the literature as the Cassie-Baxter state [17]. As expected, film flow is affected significantly by the presence of the second liquid-gas interface. The first who addressed this issue was Philip [18,19], who analytically solved the Stokes flow in an infinite channel where the no-slip condition is applied at the upper wall, while the bottom wall includes an array of longitudinal or transversal slots where the no-slip condition is applied. This has led to a simple analytical equation, which relates the effective slip length to the solid fraction of the substrate. The latter expression was validated experimentally by Ou and Rothstein [20] and Tsai *et al.* [21] using detailed microparticle image velocimetry. They have demonstrated a strong correlation between the details of the substrate with the fluid velocity in the proximity of the liquid-gas interfaces, highlighting the significance of meniscus curvature effects. Later, several researchers have tried to calculate the impact of the meniscus curvature on the macroscopic slip length, for flows in both the longitudinal and transverse directions [22–26]. In addition, the effect of the shape of the grooves on the slip length is discussed in the studies [27–29].

The Wenzel and the Cassie-Baxter states represent two extreme minima in the free energy of the system, and these two states are separated by an energy barrier [30]. Recent studies indicate that the particular characteristics of the substrate, such as the scale and orientation of its texture, play a vital role in the formation of either Cassie-Baxter or Wenzel state [31]. However, these two mentioned states are not the only possible ones. Interestingly, Giacomello *et al.* [32] identified a plethora of metastable states in which the film partially enters inside the cavities. They showed that a depinning of the inner free surface from the edges of the cavity is possible, while the free surface may form moving contact lines with the sidewalls of the grooves or bubble formation inside the microcavities of the substrate. A similar effect was also seen in the numerical study by Karapetsas *et al.* [33], who examined the motion of droplets on superhydrophobic surfaces. In the context of film flows over partially wetted structured surfaces, Pettas *et al.* [34] and Varchanis *et al.* [35] performed steady-state calculations and have shown that the presence of a moving contact line along the sidewalls of the trenches and the deformability of the liquid-gas interface leads to the existence of multiple steady configurations, due to the nonlinear dynamics of the flow, which are typically connected via a hydrodynamic hysteresis loop. These results have also been confirmed by Lampropoulos *et al.* [36] and Karapetsas *et al.* [37], who examined the dynamics of partial wetting of a substrate with rectangular trenches by performing time-dependent simulations in two and three dimensions, respectively.

Another typical characteristic of film flows is the appearance of wavy interfacial instabilities, which in the presence of substrate topography can be enhanced or mitigated by the flow conditions

and the specific characteristics of the substrate structure. Early efforts to investigate the flow instabilities of a film over a flat substrate were reported by Benjamin [38] and Yih [39]. They showed that the flow becomes unstable primarily to long-wave disturbances above a critical value of the flow rate, which depends on the inclination angle and the liquid viscosity. Their analysis predicted that for vertical substrates, the flow is unstable even under creeping flow conditions. Surface tension, on the other hand, stabilizes the flow with an increasing effect for disturbances with smaller wavelengths. To date, several research groups have examined the stability of flowing films over fully wetted substrates for several different setups, e.g., liquid with complex rheology, surfactant-laden films, or flows over structured solid surfaces, both theoretically and experimentally; see [40–48]. To take into account the fact that gas may be trapped in the microstructure of the substrate, inducing an effective slip on the flow, Samanta *et al.* [49] consider the problem of gravity-driven film flow on a slippery plane. They found that the slip at the liquid-wall interface destabilizes the flow, affecting mainly the mean velocity of the film. However, such idealized considerations reveal only part of the story and, in many cases, are not sufficient due to the effect of a curved free surface, which cannot be neglected. Arguably, the presence of a second gas-liquid interface, which is also a moving boundary, may have a considerable effect on the stability of the film, especially in cases where the film height will be comparable with the size morphology of the substrate.

The main goal of the present study is to examine the steady flow and its stability characteristics in cases where a film flows under the effect of gravity and fails to wet an array of periodic deep slits, resulting in the formation of a second liquid-gas interface. To this end, we will account fully for the deformability of all interfaces and consider (1) the ideal Cassie-Baxter state where the interface is deformable but remains attached to the groove edges and (2) the nonidealized cases (metastable states [30,31]) where the inner interface is detached from the edges of the grooves, forming either one or two contact lines with the sidewalls of the slit. To this end, we will derive a detailed theoretical model solving the momentum and mass conservation equations at steady state and performing a linear stability analysis of the calculated steady states when subjected to infinitesimal disturbances in the streamwise direction. Disturbances of arbitrary wavelengths are considered, i.e., not necessarily matching the periodicity of the substrate; this is achieved by employing the Floquet-Bloch theory. Based on the linear stability analysis results, it is possible to identify the mechanisms that lead to the strong stabilization of the flow due to the presence of air pockets inside the grooves.

The study is organized as follows: In Sec. II we give the problem formulation along with the governing equations and in Sec. III the numerical implementation. In Sec. IV we present an extensive parametric analysis to study the impact of liquid properties and geometric parameters on the steady state and the stability of the flow. Conclusions are drawn in Sec. V.

II. PROBLEM FORMULATION

We consider the steady, free-surface flow of a Newtonian liquid driven by gravity along a solid substrate. The substrate is textured with periodical slits normal to the main flow direction. In what follows, the superscript asterisk will indicate a dimensional quantity. The liquid is considered to be incompressible, with constant density ρ^* , dynamic viscosity μ^* , and surface tension σ^* . The primitive flow input is the volumetric flow rate per unit length in the z coordinate, q^* . The geometric characteristics of the topography and the film are presented in Fig. 1. For slits with a sufficiently small width, W^* , the film surpasses the groove, failing to coat the slit, forming a second interface, which is bounded by the sidewalls of the cavity. As shown in the figure, the total length of the periodic part of the substrate is denoted by L^* , while L_1^* and L_2^* correspond to the inflow and outflow length of the unit cell, respectively; therefore, the length of the solid part of the substrate is $(L_1^* + L_2^*)$. The shape of the inner free surface, as well as the wetting length of the substrate sidewalls, are highly dependent on the width of the slit, W^* . In the extreme case where the trench width is sufficiently small, the inner interface may remain pinned at the corresponding edges of the topography, entrapping air inside the cavities of the substrate; this is the so-called Cassie-Baxter state [17]; see Fig. 1(a). Under conditions, e.g., larger slit widths, the film may partially wet the

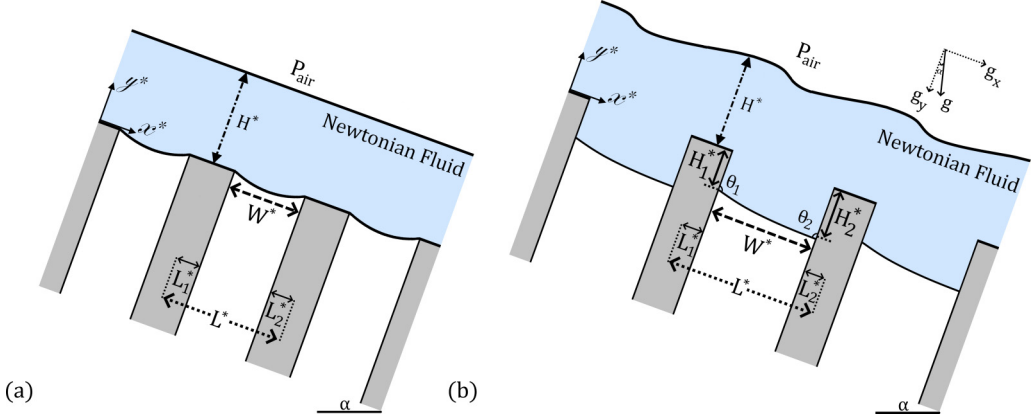


FIG. 1. Cross section of a film flowing over an inclined substrate featuring periodic slits in (a) ideal Cassie-Baxter state and (b) partial wetting configuration. In both cases, the unit cell of the periodic structures has a length L^* , and L_1^* and L_2^* denote the inflow and outflow length of the unit cell, respectively; the length of the solid part of the substrate is $(L_1^* + L_2^*)$. The gap of the slit has a width W^* , while the film height at the inlet of the periodic domain is denoted by H^* . Note that H^* is not constant since it depends on the flow rate and material parameters and will be calculated as part of the solution. The angle of the substrate inclination is denoted by α , while θ_1 and θ_2 correspond to the contact angles between the solid wall and the inner liquid-air surface. In (b) H_1^* and H_2^* indicate the distance of the contact lines along the upstream and downstream slit walls from the corresponding edges.

sidewalls of the groove, forming two contact angles with the sidewalls of the cavity, θ_1 and θ_2 ; see Fig. 1(b). In all cases, it is assumed that the topographical structures are sufficiently deep, and therefore the pressure of the encapsulated air is not affected by the degree of wetting of the grooves and therefore the ambient air pressure is maintained; the latter assumption is necessary in the case of a 2D configuration examined herein but is also relevant for a pillar/groove situation in a 3D configuration.

The origins of the cartesian coordinate system are located at the entrance of the periodic flow domain, with the x axis and y axis in the direction parallel and normal to the wall at $x = 0$, respectively. All the velocity components are scaled with the mean Nusselt film velocity, U_N^* , defined as

$$U_N^* = q^{*2/3} \left(\frac{\rho^* g^* \sin(a)}{3\mu^*} \right)^{1/3}, \quad (1)$$

while all lengths are scaled with the capillary length scale of the liquid, l_c^* :

$$l_c^* = \left(\frac{\sigma^*}{\rho^* g^*} \right)^{1/2}. \quad (2)$$

Time is scaled with l_c^*/U_N^* , while the pressure and stress components are scaled with the viscous scale $\mu^* U_N^*/l_c^*$. Introducing the above characteristic scales, the dimensionless numbers that arise in the governing equations are the Reynolds number Re , Kapitza number Ka , and inclination angle α ; their definition is given in Table I.

At this point, it is also convenient to define an additional parameter that compares the geometric characteristics of the inflow and outflow region of the unit cell with the width of the groove, labeled Tr :

$$Tr = \frac{L_1^* + L_2^*}{W^*}. \quad (3)$$

TABLE I. Dimensionless parameters and their representative values.

Dimensionless quantity	Symbol	Definition	Representative value
Reynolds	Re	$\rho^* q^* / \mu^*$	0–50
Kapitza	Ka	$\sigma^* \rho^{*1/3} g^{*-1/3} \mu^{*-4/3}$	0.1–3000
Geometric lengths	L_1, W, L_2	$L_1/l_c^*, W/l_c^*, L_2/l_c^*$	
Inclination angle	α		10° – 65°

By changing the solid fraction, Tr , while keeping constant the total length of the unit cell, we can study the effect of the topographical structures on the formation of the steady free surface. Two extreme limits arise for either large or very small values of Tr . Note that for $\text{Tr} \rightarrow \infty$ the inflow and outflow region of the domain is much larger than the trench width ($L_1 + L_2 \gg W$) and the substrate is almost flat. On the contrary, as $\text{Tr} \rightarrow 0$, the inflow and outflow regions are much smaller than the width of the groove ($L_1 + L_2 \ll W$) and the substrate tends to have a 2D pillar-like structure.

A. Governing equations and boundary conditions

The governing equations of the flow are the momentum and mass conservation equations, which in the time-dependent dimensionless form are the following:

$$\text{Re Ca}^{-1/2} \left(\frac{\sin a}{3} \right)^{1/2} \left(\frac{\partial \mathbf{u}}{\partial t} + (\mathbf{u} - \mathbf{u}_m) \cdot \nabla \mathbf{u} \right) + \nabla P - \nabla \cdot \boldsymbol{\tau} - \text{Ca}^{-1} \mathbf{g} = 0, \quad (4)$$

$$\nabla \cdot \mathbf{u} = 0. \quad (5)$$

Here $\mathbf{u} = (u_x, u_y)^T$, P , $\boldsymbol{\tau} = \nabla \mathbf{u} + \nabla \mathbf{u}^T$ denote the velocity, pressure, and stress fields in the flow domain, respectively. $\nabla = (\partial_x, \partial_y)^T$ denotes the gradient operator for a cartesian coordinate system, while $\mathbf{u}_m = \partial \mathbf{x} / \partial t$ denotes the velocity of the mesh nodes and $\mathbf{g} = (\sin \alpha, -\cos \alpha)^T$ is the unit vector in the direction of gravity. The capillary number, $\text{Ca} = \mu^* U_N^* / \sigma$, which arises in the above equation is not an independent variable but is related to the previously defined dimensionless quantities via the expression

$$\text{Ca} = \text{Ka}^{-1} \text{Re}^{2/3} \left(\frac{\sin a}{3} \right)^{1/3}. \quad (6)$$

Accounting for the boundary conditions along the free surface of the film, a local interface force balance is imposed between the normal stress and capillary forces:

$$\mathbf{n} \cdot (-P\mathbf{I} + \boldsymbol{\tau}) = -P_{\text{air}} \mathbf{n} + \text{Ca}^{-1} 2\kappa \mathbf{n}, \quad (7)$$

where \mathbf{n} is the outward unit vector to the free surfaces and 2κ denotes the mean curvature defined as $2\kappa = \nabla_s \cdot \mathbf{n}$ while $\nabla_s = (\mathbf{I} - \mathbf{nn}) \cdot \nabla$. Note that the air in contact with the interface is at the ambient air pressure, which can be set equal to zero, $P_{\text{air}} = 0$, while viscous effects in the gas phase are assumed to be negligible. Also, the interfaces obey the kinematic condition

$$\mathbf{n} \cdot (\mathbf{u} - \mathbf{u}_m) = 0. \quad (8)$$

Moreover, at the inflow and the outflow of the unit cell, periodic boundary conditions are employed. Note that at the present study, we assume that the steady flow has the same periodicity as the substrate structure (i.e., we assume that the steady solution is L -periodic):

$$\mathbf{u}|_{x=0} = \mathbf{u}|_{x=L}, \quad (9)$$

$$\mathbf{n} \cdot (-P\mathbf{I} + \boldsymbol{\tau})|_{x=0} = \mathbf{n} \cdot (-P\mathbf{I} + \boldsymbol{\tau})|_{x=L}. \quad (10)$$

Along the walls of the substrate, we impose the usual no-penetration and no-slip boundary condition:

$$\mathbf{n}_w \cdot \mathbf{u} = 0, \quad (11)$$

$$\mathbf{t}_w \cdot \mathbf{u} = 0, \quad (12)$$

where \mathbf{n}_w and \mathbf{t}_w denote the unit normal and tangential vector, respectively, to the wall. At the two intersections of the inner interface (its unit normal vectors denoted as $\mathbf{n}_{s,1}$, $\mathbf{n}_{s,2}$) with the two side walls of the slit, appropriate boundary conditions for the contact angles need to be imposed. The mobility of the contact line, though, will be taken into account by considering a slip condition at the contact line ($\mathbf{x} = \mathbf{x}_{c,i}$) adopting the following equation:

$$\beta_{cl} \mathbf{t}_{w,i} \cdot \frac{\partial \mathbf{x}_{c,i}}{\partial t} = \cos \theta_{s,i} - \cos \theta_i. \quad (13)$$

According to this model, the deviation of the dynamic contact angle, θ_i ($i = 1, 2$), from its static value, $\theta_{s,i}$ ($i = 1, 2$), provides the driving force for contact line motion; the dynamic contact angles that arise in Eq. (13) can be evaluated using $\mathbf{n}_{w,i} \cdot \mathbf{n}_{s,i} = \cos \theta_i$. Note that as the flow approaches the steady state the contact angle retrieves the usual Young (equilibrium) contact angle. This model is very similar to the Cox-Voinov model [50], widely used to model the contact line motion under the lubrication approximation, although Eq. (13) is more suitable for thick layers of fluid as in our case. We note that in the limit of very high values of β_{cl} our approach reduces to the boundary condition (i.e., perfect slip at the contact line) that has been used in Pettas *et al.* [34].

The remaining degree of freedom, the film height at the entrance of the unit cell H^* , is determined by requiring that the dimensionless flow rate is equal to unity:

$$q := \int_0^{H^*/l_c^*} u_x dy = 1. \quad (14)$$

III. NUMERICAL IMPLEMENTATION

A. Base-state–steady-state solution

The base flow is steady and 2D and is assumed to be L -periodic. In order to solve the above set of equations at a steady state numerically, we employ the mixed finite element/Galerkin method [51–53] using the arbitrary Lagrangian-Eulerian framework along with an elliptic grid generation scheme [54,55] to account for the free surface deformation. According to this technique, the physical domain (x, y) , which may assume different steady states, is mapped to a fixed computational domain (η, ξ) . The details of the implementation of this scheme for our particular setup can be found in [34,35].

B. Linear stability analysis

We consider the stability of this steady flow subjected to infinitesimal 2D perturbations. The variables are written in the computational domain and are decomposed into a part that corresponds to the base state solution and an infinitesimal disturbance using the following ansatz:

$$\begin{bmatrix} \mathbf{u} \\ P \\ \mathbf{x} \end{bmatrix} (\eta, \xi, t) = \begin{bmatrix} \mathbf{u}_b \\ P_b \\ \mathbf{x}_b \end{bmatrix} (\eta, \xi) + \delta \begin{bmatrix} \mathbf{u}_d \\ P_d \\ \mathbf{x}_d \end{bmatrix} (\eta, \xi) e^{\lambda t}. \quad (15)$$

The first terms on the right-hand side of these equations represent the steady-state solution, indicated by the subscript “ b ,” while the second ones are the perturbation. The subscript “ d ” corresponds to the spatial variation of the disturbance, while $\delta \ll 1$; \mathbf{x}_d is the disturbance of the position vector. According to our ansatz, an exponential dependence on time is assumed; here λ

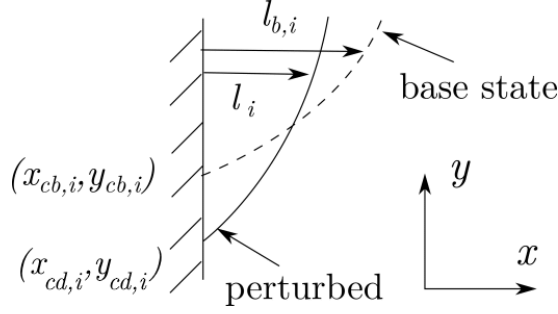


FIG. 2. Schematic of the contact line along the sidewalls depicting the side view of the base state and perturbed interface profile and definitions of l_i and $l_{b,i}$ which denote the interfacial distance from the wall. The relation between $x_{c,i}$, $x_{cb,i}$ and $x_{cd,i}$ is $x_{c,i} = x_{cb,i} + \delta x_{cd,i}$.

denotes the growth rate. If the calculated λ turns out to have a positive real part, the disturbance grows with time and therefore, the corresponding steady state is considered unstable.

Introducing the expression (15) in the weak formulation of the time-dependent governing equations and the corresponding boundary conditions (7)–(14) and neglecting terms of order higher than the first in the perturbation parameter δ , the linearized equations are derived; a detailed description is provided in Appendix A of [42].

1. Contact line

The boundary conditions applied at the contact lines ($x = x_{c,i}$) require special attention. An approach similar to that in [56] is adopted. We denote the base state position of the contact line i with $x_{cb,i}$ while its disturbance is denoted by $x_{cd,i}$ (see Fig. 2). We will also define l_i and $l_{b,i}$ to denote the distance of the liquid-air interface from the wall for the perturbed and unperturbed flow domain, respectively. Expanding l_i in a Taylor series about $y_{cb,i}$ we get

$$l_i = l_{b,i} + \delta \left[l_{d,i} + y_{cd,i} \left(\frac{\partial l_{b,i}}{\partial y} \right)_b \Big|_{y_{cb,i}} \right]. \quad (16)$$

At the contact line, the distance from the wall must be zero, which implies $l_i|_{y_{cd,i}} = l_{b,i}|_{y_{cb,i}} = 0$. Therefore from Eq. (16) we get that the amplitude of the perturbation at the base state position of the contact line is given by

$$y_{cd,i} = - \frac{l_{d,i}|_{y_{cb,i}}}{\left(\frac{\partial l_{b,i}}{\partial y} \right)_b \Big|_{y_{cb,i}}}. \quad (17)$$

Performing a similar expansion for the no-penetration condition for the velocity component normal to the wall yields

$$v_{x,d} = -y_{cd,i} \left(\frac{\partial v_{x,b}}{\partial y} \right)_b \Big|_{y_{cb,i}}. \quad (18)$$

We also expand Eq. (13) and get the expression

$$\beta_{cl} \left[\frac{\partial x_{cd,i}}{\partial t} + \frac{\partial y_{cd,i}}{\partial t} \left(\frac{\partial l_{b,i}}{\partial y} \right)_b \Big|_{y_{cb,i}} \right] = (\mathbf{n}_{w,i} \cdot \mathbf{n}_{s,i})|_d + y_{cd,i} \frac{\partial [(\mathbf{n}_{w,i} \cdot \mathbf{n}_{s,i})|_b]}{\partial y} \Big|_{y_{cb,i}}. \quad (19)$$

The latter two conditions [Eqs. (18) and (19)] in combination with the linearized kinematic condition (see Appendix A in Pettas *et al.* [42]) are sufficient to describe the contact line motion in the perturbed flow domain. In order to apply this boundary condition, we will also need to provide

an appropriate definition for both $l_{b,i}$ and $l_{d,i}$. In our case, the contact line i is located at one of the following two locations:

Either at the upstream wall, which is oriented in the y direction, and therefore, we obtain

$$l_{b,1} = x_b - x_{w,1} \quad \text{and} \quad l_{d,1} = x_d \quad (20)$$

Or at the downstream wall, which is also oriented in the y direction, and therefore, we obtain

$$l_{b,2} = x_{w,2} - x_b \quad \text{and} \quad l_{d,2} = x_d. \quad (21)$$

2. Periodic boundary conditions and implementation of Floquet-Bloch theory

For flows over periodically structured surfaces, the most unstable disturbance may have a wavelength that exceeds the period of the domain. Thus, it becomes evident that if one assumes periodic conditions for the disturbances between the inflow and outflow boundaries, the overall linear stability of the system cannot be captured unless a sufficiently long computational domain is considered. This would imply a formidable computational cost when long-wave disturbances are the most unstable ones, as is the typical case for thin-film flows. As Pettas *et al.* [42] discussed, an appropriate and efficient way to deal with this issue is to employ the Floquet-Bloch theory, which allows us to model the flow over a structured surface considering the small periodic domain of the topography. This accomplishes a considerable reduction to the computational cost while examining disturbances with wavelengths extending over multiple trenches or fractions thereof. According to Bloch's theorem [57], it is sufficient to look for solutions such that the disturbances between the inflow and outflow of the unit cell are related to each other with the following expression:

$$\begin{bmatrix} \mathbf{u}_d \\ P_d \\ y_d \end{bmatrix} \Big|_{x=0} = \begin{bmatrix} \mathbf{u}_d \\ P_d \\ y_d \end{bmatrix} \Big|_{x=L} e^{2\pi Q i}. \quad (22)$$

Using this formulation, the unknown disturbances (\mathbf{u}_d , P_d , y_d) will be determined by imposing Eq. (22) at the edges of the periodic domain, ensuring that for finite real values of Q , the disturbances will not be L -periodic. As discussed in Pettas *et al.* [42], it is sufficient to examine the values of $Q \in [0, 0.5]$. For example, when $Q = 0.5$, the imposed perturbation has a wavelength that is twice the size of the physical domain, whereas $Q \rightarrow 0$ corresponds to disturbances with a wavelength much larger than the size of the periodic domain. Disturbances with $Q = 0$ should be distinguished since, in that case, Eq. (22) reduces to typical periodic boundary conditions. Thus, this case corresponds to disturbances with the same period or aliquots of the basic solution, i.e., correspond to superharmonic instabilities.

3. The Arnoldi algorithm

After we discretize the linearized set of equations, we end up with a generalized eigenvalue problem of the form

$$\mathbf{A}\mathbf{w} = \lambda \mathbf{M}\mathbf{w}, \quad (23)$$

where \mathbf{A} and \mathbf{M} are the Jacobian and the mass matrix, respectively, with λ the eigenvalues and \mathbf{w} the corresponding eigenvectors. This eigenvalue problem is solved using Arnoldi's method combined with the shift-and-invert transformation, which allows us to locate only the eigenvalues of interest; for determining critical conditions, we need those eigenvalues with the smallest real part [53,58–60]. According to our framework, the solution is stable if the real parts of all eigenvalues are less than or equal to zero for all values of Q . To implement Arnoldi's algorithm, we use the public domain software ARPACK [61] while the accuracy of the converged eigenpairs is independently checked by evaluating the residual $|\mathbf{A}\mathbf{w} - \lambda \mathbf{M}\mathbf{w}|$. This quantity is always less than 10^{-12} for the reported results. The methodology for the eigenvalue calculation is described in detail in the studies of Karapetsas *et al.* [59] and Pettas *et al.* [42].

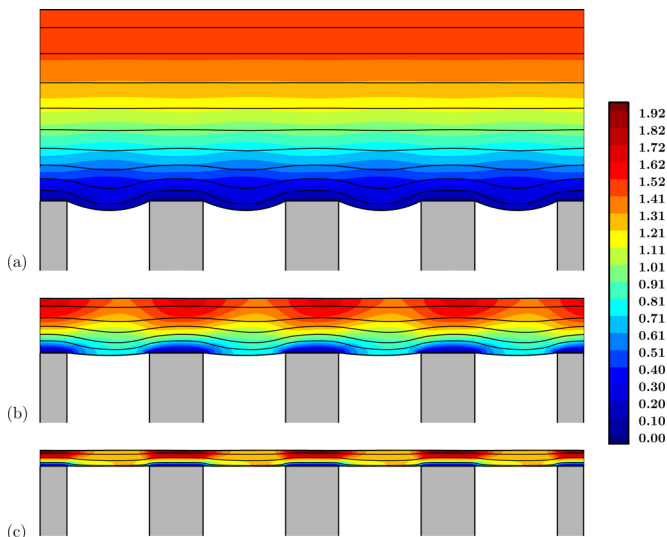


FIG. 3. Streamlines and the spatial variation of v_x for (a) $Ka = 10$, (b) $Ka = 100$, and (c) $Ka = 1000$. The remaining parameter values are $Re = 5.5$, $\alpha = 10^\circ$, and the film thickness for each liquid is 1.39, 0.39, and 0.11, respectively.

IV. RESULTS AND DISCUSSION

The accuracy of our numerical results is verified by performing a series of validation tests of our in-house code with theoretical predictions for relevant flows found in the literature. These tests are reported in the Appendix. Moreover, all results presented below have converged with mesh refinement. Numerical solutions were obtained over a wide range of parameter values. The “base” case, however, has typical dimensionless values of $L = 1$, $L_1 = L_2 = 0.20$, and $W = 0.60$; then from Eq. (3), $Tr = 0.67$. In the case of partial wetting, the contact angle is $\theta_1 = \theta_2 = 120^\circ$ at the base state. This set of parameters will be kept constant throughout the paper unless stated otherwise.

A. Ideal Cassie-Baxter state: Steady state

We begin our discussion by examining the stability of the ideal Cassie-Baxter state, where the inner liquid-air interface does not wet the slit sidewalls and the contact lines remain pinned at their edges. In Fig. 3 we present the spatial variation of v_x for the steady flow of three different Newtonian liquids with $Ka = 10$, 100, and 1000, respectively. It is anticipated that this state could be observed experimentally in cases where the length of the grooves is smaller than the size of the capillary length scale so that the surface tension force can support the pinning of the inner interface at the edges of the substrate. In the present case, the dimensional width of the gap in Fig. 3 is $\sim 600 \mu\text{m}$, whereas the capillary length of the liquid is $l_c^* \sim 1 \text{ mm}$ and therefore the above condition is met. Since surface tension and density do not vary considerably (l_c^* is nearly constant), the variation of Ka corresponds to liquids with different viscosity. For liquids with high viscosity [e.g., see Fig. 3(a) for $Ka = 10$], away from the substrate the streamwise velocity component, v_x , does not vary significantly in the x direction due to the large height of the liquid film. The maximum value of v_x (located at the outer interface) is found to be a 1.49, indicating that the film surface velocity approximates the corresponding value of the flow over a flat substrate ($U_{s,N} = 1.50$, with the nondimensionalization we used). On the other hand, the velocity in the proximity of the inner interface is very small. Hence, the normal force balance at the inner interface is reduced to the

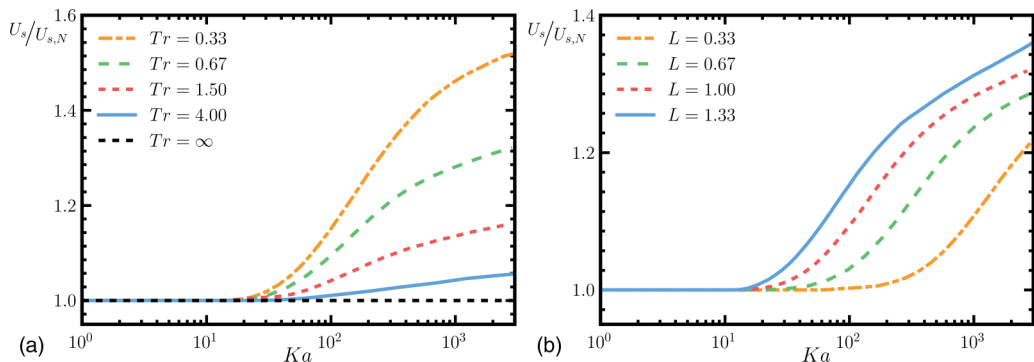


FIG. 4. The maximum interfacial velocity, U_s , normalized by the surface velocity of simple Nusselt flow as a function of Ka for various values of (a) the slit width, W , for $L = 1$, and (b) the length of the unit cell, L , for $Tr = 0.67$. The remaining parameter values are $Re = 5.5$ and $\alpha = 10^\circ$.

Young-Laplace equation:

$$\Delta P \approx \frac{1}{Ca} 2\mathcal{H}. \quad (24)$$

Therefore, the positive curvature of the inner interface could mainly be attributed to the hydrostatic pressure in that region.

Moreover, as shown in Fig. 3, with increasing values of Ka , the film thickness decreases due to the higher velocity of the liquid; we find that $H^* = 1.39 l_c^*$, $0.39 l_c^*$, and $0.11 l_c^*$ for $Ka = 10$, 100 , and 1000 , respectively. For $Ka = 100$, the decreased film thickness leads to a 2D profile of v_x which is nearly parabolic in regions above the solid parts of the substrate and nearly flat above the slits. In the latter regions, an almost shear-free region is formed where the fluid is, on the one hand, accelerated by gravity and, on the other hand, feels less resistance by the solid substrate, thereby increasing the overall fluid mobility. This can be seen for the case with $Ka = 1000$ where the maximum value of v_x is found to be 1.92 , denoting that the velocity field obtains significantly higher values than in Nusselt flow.

To elucidate the impact of the substrate topography on the steady flow, we present in Fig. 4 the maximum interfacial velocity, U_s normalized by the surface velocity of simple Nusselt flow ($U_{s,N}$) as a function of Ka ; the value of Re is equal to 5.5 for all cases shown in this figure. In Fig. 4(a) we present the effect of the geometric ratio, Tr , while the total length of the unit cell is set to $L = 1$; the black dashed line corresponds to the case where the substrate is perfectly flat; thus, the velocity field is identical to the Nusselt flow. As expected, for large values of Tr [small slit widths; see Eq. (3)], the presence of the second interface has a small impact on the fluid flow, and small deviations from Nusselt flow are observed for even high values of Ka (as high as $Ka \sim 100$). Higher values of Ka correspond to liquids with lower viscosity allowing for the easier formation of a plug flow region above the slits, enhancing the mobility of the liquid film. For substrates with large slit widths (i.e., for low values of Tr), this effect becomes more pronounced; namely, for $Ka = 2000$, the normalized maximum interfacial velocity is calculated to be 1.05 , 1.16 , 1.32 , and 1.52 for $Tr = 4.00$, 1.50 , 0.67 , and 0.33 , respectively. For the lowest value of Tr that we have examined ($Tr = 0.33$), the substrate has a pillared structure since the gap is three times larger than the width of the flat rigid solid. We also observe that for all values of Tr an asymptotic limit arises for $Ka \sim 20$, and below that threshold, the maximum velocity at steady state becomes approximately equal to $U_{s,N}$ denoting that the steady surface velocity is not affected by the presence of the topographical morphologies.

The impact of the total length of the unit cell on the flow field is depicted in Fig. 4(b), where we have set a constant value of $Tr = 0.67$ and vary the length of the unit cell, L , by choosing appropriate

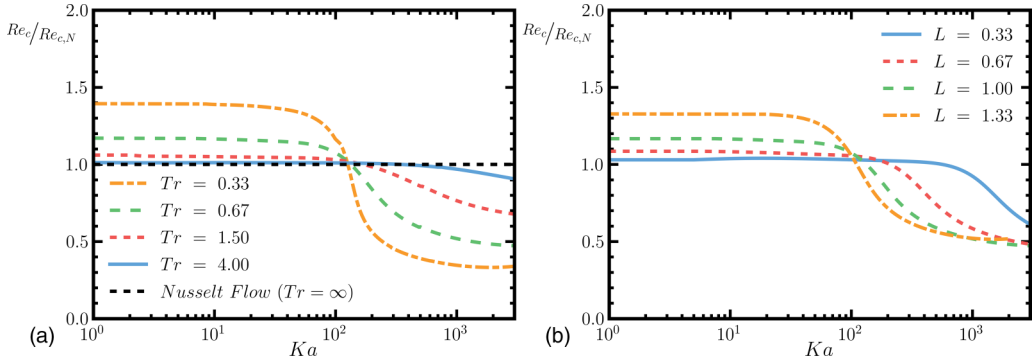


FIG. 5. Critical Re_c as a function of Ka for (a) various values of Tr and for $L = 1$ and (b) various values of L and for $Tr = 0.67$. The other parameter value is $\alpha = 10^\circ$.

values for the geometrical parameters L_1 , L_2 and W . All the curves shown in Fig. 4(b) reach an asymptotic limit for $Ka < 20$, where the maximum interfacial velocity becomes independent of the length of the unit cell. This limit corresponds to a flow dominated by viscous dissipation that takes place along the flat rigid solid surface of the substrate. For higher values of Ka , the maximum interfacial velocity depends strongly on the substrate topography, since the larger the length of the slit is, the more effective the transition to the “stick-slip” regime will be [8], denoting that the length of the inner free surface drastically affects this transition. These observations also help us draw some conclusions regarding the effect of the substrate topography and the liquid properties on the drag force reduction for flows over substrates with slits, which is related to enhancing the interfacial velocity of the liquid film. We deduce that the macroscopic drag force coefficient for low values of Ka is not affected significantly by the substrate topography, whereas for very high values of Ka it is affected only by the relative ratio of the topographical distances, i.e., the geometric parameter Tr , and is not affected significantly by the length of the unit cell.

B. Ideal Cassie-Baxter state: Linear stability

Next, we turn our attention to the stability of the flowing film in the ideal Cassie-Baxter state when subjected to infinitesimal, 2D disturbances. In Fig. 5(a) we present the critical Reynolds number of the previously mentioned steady states subjected to long-wave disturbances ($Q = 10^{-2}$) as a function of Ka for various values of Tr ; the black dashed line corresponds to the critical conditions of the flow over a flat substrate. As shown in this figure, the shape of the substrate structures may considerably affect the stability of the system over the entire range of Ka , depending on the value of the geometrical parameter, Tr . As we have already seen in the previous section, the inner interface does not significantly affect the steady velocity profile for low values of Ka (high viscosity liquids). Nevertheless, its effect on flow stability appears to be dramatic. For narrow slits (high values of Tr), the critical Re_c for $a = 10^\circ$ tends asymptotically to the prediction obtained by Benjamin [38] for Nusselt flow; see the Appendix. With decreasing Tr , though, the flow is stabilized with considerable increase of Re_c for the onset of the instability; for $Ka = 1$ the critical values of the Reynolds number were calculated to be $Re_c = 4.73, 4.78, 5.01, 5.53, 6.57$ for $Tr = \infty, 4.0, 1.5, 0.67, 0.33$, respectively. For a constant unit length, a decrease of Tr corresponds to slits with relatively larger width, W , and an increased length of the inner interface which also renders it more flexible. Therefore, it is reasonable to assume that for highly viscous liquid films, the presence of a flexible inner interface acts as a damper that absorbs the disturbances that arise at the external interface.

On the other hand, with increasing Ka values (decreasing liquid viscosity), the interface becomes less flexible [the local value of the capillary number decreases; see Eq. (6)], and, therefore, the

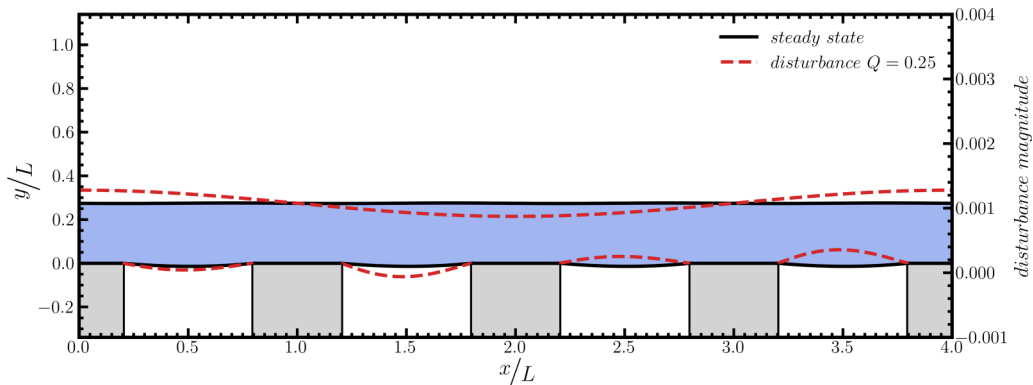


FIG. 6. Free-surface disturbances for $Q = 0.25$ which corresponds to an unstable mode of the Cassie-Baxter state for $Re = 10$ and $Ka = 100$. The corresponding eigenvalue is $\lambda = 0.053 + 1.249 i$. The geometric parameter is $Tr = 0.67$ and $L = 1$, while the inclination angle is $\alpha = 10^\circ$.

stabilizing effect of the inner interface becomes less important. Besides, the accelerated film flow due to the reduction of the macroscopic drag coefficient renders inertial effects increasingly important. As a result, we find that for moderate values of Ka ($Ka > 60$), the critical Re decreases considerably with the increase of Ka ; see Fig. 5(a). Due to the higher base state interfacial velocities in the shear-free region and the effect of inertia, the disturbances propagate more efficiently in the streamwise direction. As expected, this effect also depends on the length of the inner interface with larger slit widths (for lower values of Tr), leading to flow destabilization. For very high values of Ka , though, Re_c reaches an asymptotic limit which is more clearly seen for the case of $Tr = 0.33$ [see Fig. 5(a)]. This can be attributed to the fact that the maximum interfacial velocity at the base state also reaches an asymptotic value in this limit, thereby posing a saturation limit on the effect of inertia. For very high Ka values, the critical conditions for instability are determined primarily by the geometrical parameter Tr ; for $Ka = 2000$ the calculated critical value of the Reynolds number is $Re_c = 4.25, 3.21, 2.22$, and 1.60 for $Tr = 4.0, 1.5, 0.67$, and 0.33 , respectively.

In Fig. 5(b) we also examine the critical conditions in the case where the substrate maintains the same geometrical ratio, $Tr = 0.67$, i.e., keeping the same analogy between solid parts of the substrate and shear-free zones, while varying the length of the unit cell. Based on the above discussion, it is anticipated that the presence of the entrapped air inside the grooves of the substrate stabilizes the fluid flow for low values of Ka and destabilizes it at high values of Ka , which is seen in Fig. 5(b). Moreover, in the latter limit, the critical Reynolds number reaches an asymptotic limit independent of L .

The disturbed flow and interfacial profile can be visualized looking at the eigenvector of the corresponding mode. In Fig. 6 we present the most unstable eigenmode for $Re = 10$ and $Ka = 100$. For visualization purposes we consider a case for which the base state flow is subjected to long-wave disturbances with $Q = 0.25$, i.e., for a disturbance which is $4L$ periodic; the visualization of the perturbed flow is easier than for the case examined in Fig. 5 (i.e., for $Q = 10^{-2}$), which corresponds to a disturbance with 100 times larger wavelength than the regular unit periodic cell of the substrate. In Fig. 6 the solid black lines represent the steady-state shape of the film and the red dashed lines the disturbances of the film. It is found that for the most unstable mode traveling waves are produced at the external interface of the film flow, while the inner interfaces are deflected in accordance with these disturbances.

So far, we have discussed the stability of the steady flow of a film in the ideal Cassie-Baxter state, allowing only long-wave disturbances, i.e., for $Q \ll 1$. To investigate the effect of disturbances with any wavelength, hereafter we will also present stability maps (e.g., see Fig. 7) considering values of the Bloch wave number Q in the range $[0, 0.5]$; as noted in Pettas *et al.* [42], this range is necessary

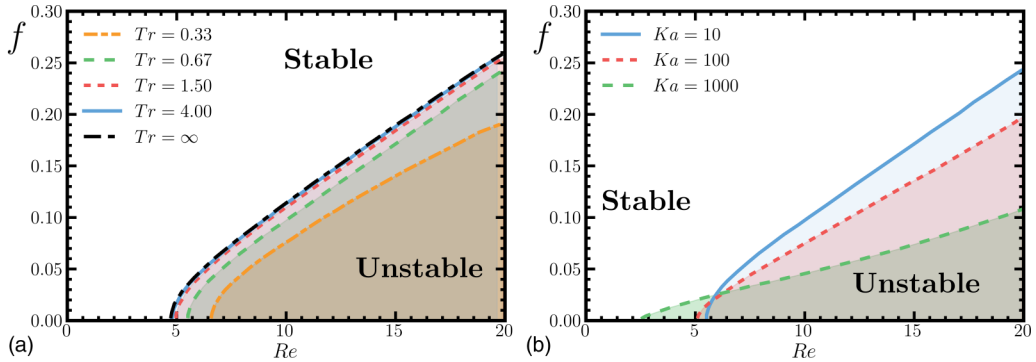


FIG. 7. Stability diagrams for (a) $Ka = 10$ and different values of Tr , (b) $Tr = 0.67$ and different values of Ka . The remaining parameter values are $L = 1$ and $\alpha = 10^\circ$.

and sufficient for calculating the total spectrum. The stability maps, though, are presented in the (Re, f) plane. The latter representation is preferable [compared to stability maps in the (Re, Q) plane often found in the literature], having the advantage that the theoretical predictions can be directly compared with experimental observations.

Figure 7(a) presents the stability map for $Ka = 10$ and different values of Tr . The discontinuous lines correspond to the neutral curves, which separate the stable from the unstable regimes, whereas the shadowed areas correspond to the regime of unstable steady states; the black dashed line corresponds to the neutral curve of Nusselt flow. In the (Re, f) the plane, all curves exhibit a semiparabolic profile denoting that the flow is stabilized with disturbances of increasing frequency, which can be attributed to capillary forces tending to stabilize any high-frequency distortions of the free surface; see D'Allesio *et al.* [62]. In line with the findings that we have discussed in Fig. 5 for long-wave disturbances, we find that even for perturbations of finite wavelength decreasing the value of the geometrical parameter Tr (which for a constant length of the unit cell corresponds to increase of the slit width) the corresponding neutral curves are shifted to higher values of the Reynolds number, indicating that the presence of the shear-free regions stabilizes the flow.

In Fig. 7(b) we set $Tr = 0.67$ and examine the stability maps for three different values of Ka , representing cases of liquids with decreasing viscosity. Under long-wave conditions (i.e., $f \rightarrow 0$), we clearly see the destabilization of the flow as discussed in Fig. 5(a). However, we observe that beyond some critical frequency of the disturbances ($f > 0.025$), a different picture emerges and the flow becomes stabilized with increasing Ka ; e.g. for disturbances with frequency $f = 0.05$ the critical conditions were calculated to be $Re_c = 6.99, 7.91, 10.75$ for $Ka = 10, 100$, and 1000 , respectively. This behavior can be understood by considering that we have two competing mechanisms affecting the flow stability of the system. On one hand, increasing Ka (decreasing liquid viscosity) inertia becomes more important due to the induced faster film flow in the shear-free region (see discussion of Fig. 4), tending to destabilize the flow. Hence, the impact of the slit is more prominent to the fluid flow, shifting the velocity field to higher values. On the other hand, with decreasing liquid viscosity, the local capillary number at the interface decreases (it cannot be counterbalanced by the corresponding increase of the interfacial velocity), denoting the increasing importance of capillary forces with decreasing wavelength of the disturbances. Clearly, for long-wave disturbances, inertia wins the competition leading to destabilization of the flow. For disturbances with sufficiently high frequency, though, the high curvature of the liquid-gas interface will intensify the effect of capillary forces, ultimately leading to stabilization of the flow.

To complete our parametric study for ideal Cassie-Baxter state, we investigate the effect of the inclination angle on the stability of the fluid flow. In Fig. 8 we present the stability diagram for a film flowing over a substrate inclined at $\alpha = 10^\circ, 25^\circ, 40^\circ, 60^\circ$ with respect to the horizontal position. Note that in the case of the flat film, the analytical expression for critical Reynolds [see Eq. (A1)

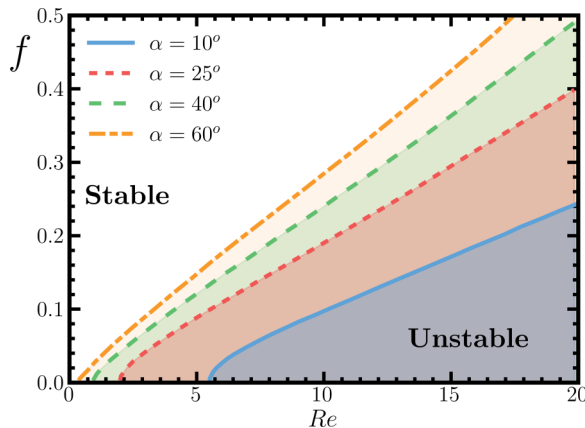


FIG. 8. Effect of inclination angle in the stability diagrams for $Ka = 10$, $L = 1$ and $Tr = 0.67$.

in the Appendix] indicates that the flow is destabilized with increasing α , and for $\alpha = 90^\circ$ the flow becomes unstable at exactly $Re_c = 0$. Indeed, in Fig. 8, as the inclination angle increases, the flow is destabilized since the gravity component in the direction of the flow increases proportionally. The most critical value of Re was calculated to be 5.45, 1.96, 0.93, 0.39 for $\alpha = 10^\circ$, 25° , 40° , and 60° , respectively. However, in contrast to the film flow over flat surfaces, for this specific configuration we find that at $\alpha \sim 63^\circ$ the flow field becomes unstable at $Re_c = 0$. Therefore, for $\alpha > 63^\circ$ it is unconditionally unstable under long-wave distortions.

C. Partial wetting

Now we turn our attention to cases where the edges of the inner interface do not necessarily remain attached to the edges of the solid substrate (ideal Cassie-Baxter state). As mentioned, these types of flows are considered metastable between the two extreme states, Wenzel and Cassie-Baxter [32]. It is anticipated that such flow configurations may be preferable for slit widths that exceed the capillary length of the liquid ($W^* > l_c^*$). Pettas *et al.* [34] showed that when the film partially wets a substrate, multiple steady-state solutions might arise connected via turning points while different amounts of liquid can be supported inside the slit. According to this paper, four different steady states may coexist under the same flow rate. Hence, the stability analysis of this system is rather complicated due to the appearance of multiple steady solution families. As a starting point, we will examine first the most general case where the film may partially wet both sidewalls of the slit [see Fig. 1(b)] and then proceed to investigate the case where the film remains attached to the edge of the upstream wall (i.e., no wetting of the upstream wall) and partially wets the downstream wall. The latter state is of particular interest since it has been shown by Lampropoulos *et al.* [36], who performed transient simulations of gravity-driven Newtonian films over substrates with rectangular topographical features, that such steady states may be encountered; e.g., see Fig. 18 in the Appendix.

1. Partial wetting of both sidewalls

Initially, we consider a case where the film partially wets both the upstream and downstream groove walls. Here, we will only briefly discuss the main characteristics of the steady state and proceed with the linear stability analysis results; the interested reader may refer to the study of Pettas *et al.* [34] for additional information regarding the steady-state solutions.

In Fig. 9(a) we present the wetting distance at the upstream wall, H_1 , as a function of the dimensionless flow rate. We observe that for low values of Re the film penetrates deep inside the topographical feature and the wetting distance at the upstream wall, H_1 , increases considerably as the flowrate decreases. On the other hand, the wetting distance at the downstream wall, H_2 , is always

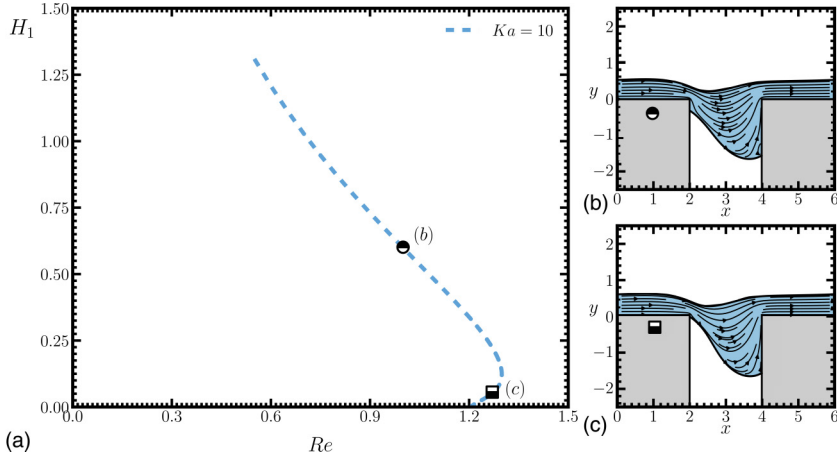


FIG. 9. (a) Wetting length H_1 as a function of Re , for $W = 2$, $L_1 = 2$, $L_2 = 2$, $\alpha = 60^\circ$, and $\theta = 120^\circ$. (b), (c) steady-state formation and streamline pattern that corresponds to the upper [(b), $Re = 1$] and lower branch [(c), $Re = 1.27$] of panel (a), respectively.

greater than H_1 ; see Figs. 9(b) and 9(c). Increasing Re to moderate values, the wetting distance decreases progressively as the upstream wall becomes dewetted; typical steady-state patterns of the upper solution family are presented as insets in Figs. 9(b) and 9(c). Finally, at $Re \sim 1.35$, partial wetting cannot be supported by the flow and a turning point arises; in fact, it is depicted in this figure that in the range of $1.20 < Re < 1.35$ multiple steady-state solutions arise. The upper branch corresponds to somewhat more successful wetting of the upstream wall, whereas, for the lower branch, the contact line at the upstream wall is somewhat closer to the upstream convex corner of the substrate; see Fig. 9(c). Nonetheless, we should also note that for $Re < 1.20$, a state of complete dewetting of the upstream sidewall ($H_1 = 0$) is also possible; such cases have been seen in transient simulations by Lampropoulos *et al.* [36] (e.g., see Fig. 18 in the Appendix), were later confirmed by Pettas *et al.* [34], and will be examined in Sec. IV C.

To determine the stability of the two solution branches, we present in Figs. 10(a) and 10(b) the eigenspectra for two steady states that lie at the upper and lower branch, respectively [see Figs. 9(b) and 9(c)]. The spectrum consists of one open branch and two closed isolated loops [marked inside the red ellipses in Fig. 10]; spectra with similar structure were also shown in Tseluiko *et al.* [63].

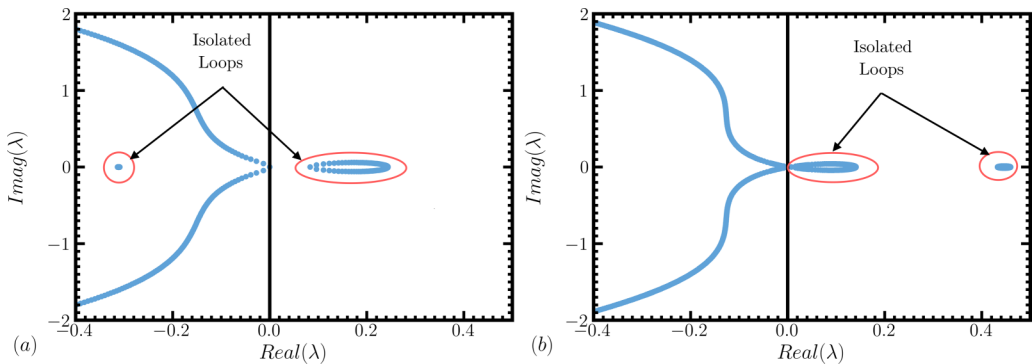


FIG. 10. (a), (b) Eigenspectra for the corresponding steady states of Figs. 9 (b) and 9(c), respectively. $Q \in [0, 0.5]$.

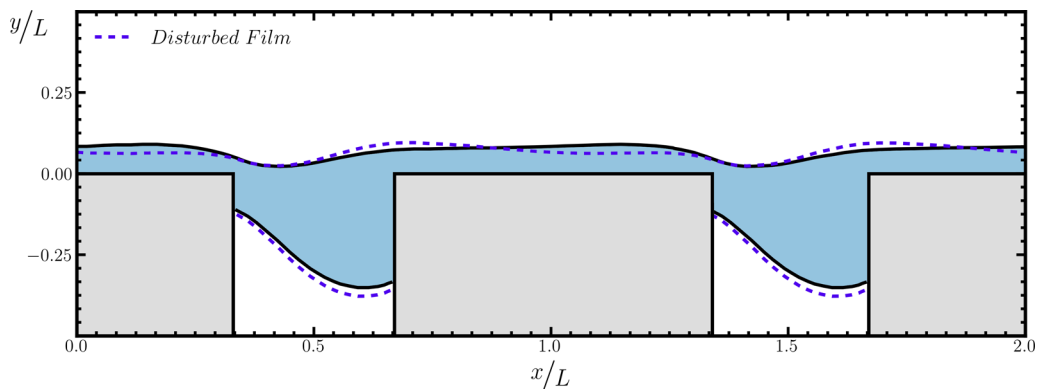


FIG. 11. Steady (black lines) and perturbed (red dashed lines) film shape for $Re = 1.27$, $Ka = 10$, $L_1 = L_2 = 2$, $W = 2$, $\alpha = 60^\circ$. The perturbed film shape results from the superposition of the steady film and the disturbance that corresponds to the most unstable mode, i.e., for $Q = 0$, $\lambda = 0.24 + 0.00i$.

In Fig. 10(a) we observe that the open branch of the spectrum consists of eigenvalues, which all have a negative real part and, therefore, the corresponding modes are stable. However, this is not the case for the eigenvalues which are part of the rightmost isolated loop. In this part of the spectrum the most unstable eigenvalue is real with a positive real part, $\text{Real}(\lambda) = 0.24$; this mode arises for $Q = 0$ and therefore corresponds to disturbances with the same period or aliquots of the unit cell of the substrate. Moreover, since the imaginary part of the most unstable eigenvalue is zero, the disturbances exponentially grow in time, indicating that the flow is subjected to a “nonoscillatory” instability. With increasing values of Re , the most unstable eigenvalue is shifted to larger positive values and therefore the system becomes even more unstable.

To understand the nature of this type of instability, we present in Fig. 11 both the steady film shape (continuous black line) along with the perturbed interface that corresponds to the most unstable mode (red dashed lines); the latter has been produced by amplifying the magnitude of the disturbance 100 times and superposing it to the steady film shape. From this figure, it becomes apparent that the disturbed flow primarily affects the inner interface by forcing the film to intrude deeper inside the topographical features of the substrate. To shed some light on the mechanism for the destabilization of the flow, we focus on the primary forces acting upon the film. Gravity acts both in the streamwise and transverse direction of the flow (inclined substrate), and due to the latter, gravity pushes the film inside the slit. The capillary force (resisting the deformation of the inner interface) in collaboration with the force acting at the two contact lines (since the walls are hydrophobic) supports the liquid column and counteracts the gravitational force. As shown in Fig. 11, the inner interface deforms, primarily near the downstream wall in the perturbed state. However, enhanced wetting at the downstream wall leads to increased hydrostatic pressure near the contact line, inevitably assisting wetting. Additionally, the deformation of the inner interface will also increase the contact angle at the upstream wall, which will facilitate wetting to reestablish the equilibrium contact angle. Therefore, this type of disturbance will destabilize the flow as there is practically no restoring mechanism. Alternatively, if the disturbance happens in the opposite direction, the unbalanced capillary force at the contact line, due to the decreased effect of the hydrostatic pressure, will eventually drive the liquid out of the slit.

Examining the stability of the steady solution of the lower branch [Fig. 9(c)], we find a similar picture as discussed above. The eigenspectrum for this case is presented in Fig. 10(b) and reveals that the most unstable eigenvalue is also real with a positive real part [$\text{Real}(\lambda) = 0.46$] and arises for $Q = 0$, as well. These results indicate that both solution branches are unstable since, in each case, there is at least an eigenvalue that is real and positive, and, therefore, neither of these two steady states (where the film forms two contact lines with the sidewalls) can be observed in an experiment.

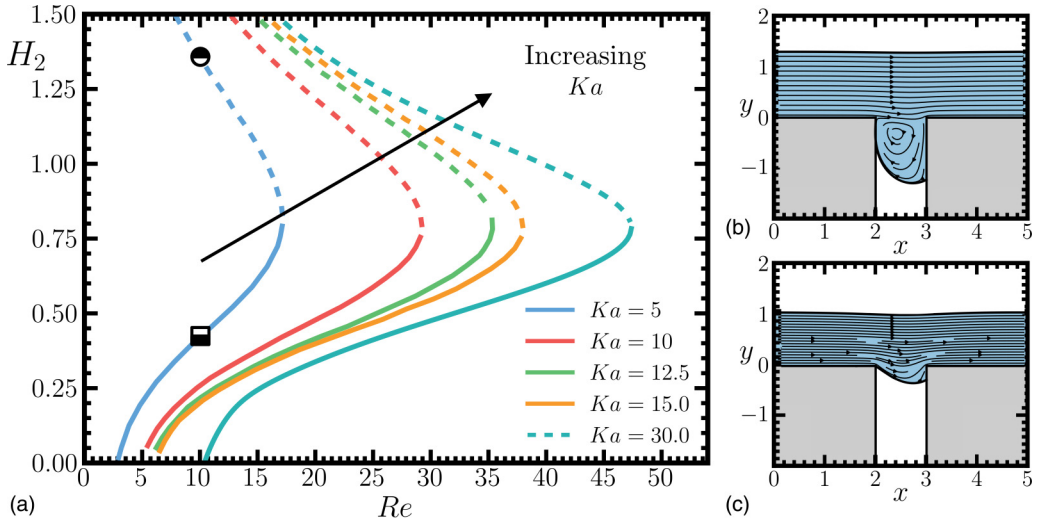


FIG. 12. (a) Wetting length H_2 as a function of Re for different values of Ka and $W = 1$, $L_1 = 2$, $L_2 = 2$, $\alpha = 60^\circ$ and $\theta = 120^\circ$. Panels (b) and (c) correspond to indicative flow configurations shown with points in panel (a).

It is important to note that this statement is true only when considering film flows over very deep periodical slits. For cases where the trenches have finite depth, in principle, the entrapped air could have different pressure than the ambient air pressure contributing to an additional stabilization mechanism. This investigation, however, is outside the scope of the present work.

2. Partial wetting only at the downstream wall

a. Base state

We have established in the previous section that steady-state solutions where the film partially wets both sidewalls are not stable. As already noted, another possible state would be that of a liquid film partially wetting only the downstream wall with complete dewetting of the upstream wall ($H_1 = 0$). As a result, the first triple contact point will always be pinned at the upstream convex corner of the slit, while the second triple contact point is free to move along the downstream sidewall.

Figure 12(a) presents the wetting distance at the downstream wall, H_2 [see Fig. 1(b)] as a function of Re , while Figs. 12(b) and 12(c) indicate some typical steady film shapes and streamline patterns of the two solution branches; the steady-state curves were obtained assuming $\beta_{cl} = 0$, to simulate the case of a fully mobile contact line. Our first observation is that this flow configuration can be sustained for much higher flow rates, i.e., for $Ka = 10$, steady solutions exist up to $Re \sim 29$ in contrast with the previous flow configuration (both sidewalls partially wetted) where steady solutions were not found for $Re > 1.35$. As shown in Fig. 12(a), the solution curve can be split into an upper and a lower solution branch connected via a turning point (for $Ka = 10$ the turning point arises at $Re \sim 29$). The upper solution branch corresponds to the case of deep penetration of the film in the cavity as seen in Fig. 12(b). As shown in this figure, the interface becomes highly deformed following closely the upstream wall, while the contact line remains pinned at the upstream corner; for lower values of Re , though, an air inclusion near the upstream corner may form; such cases are not examined herein. The flow field consists of an outer region where the liquid flows downstream due to gravity and an inner region inside the slit where a weak recirculation exists in the encapsulated liquid which remains almost stagnant; see also the relevant discussion by Pettas *et al.* [34]. Increasing the flow rate (and thus Re), the wetting length H_2 decreases considerably, indicating that the film dewets the downstream wall of the slit, up to a critical value of Re where a turning point

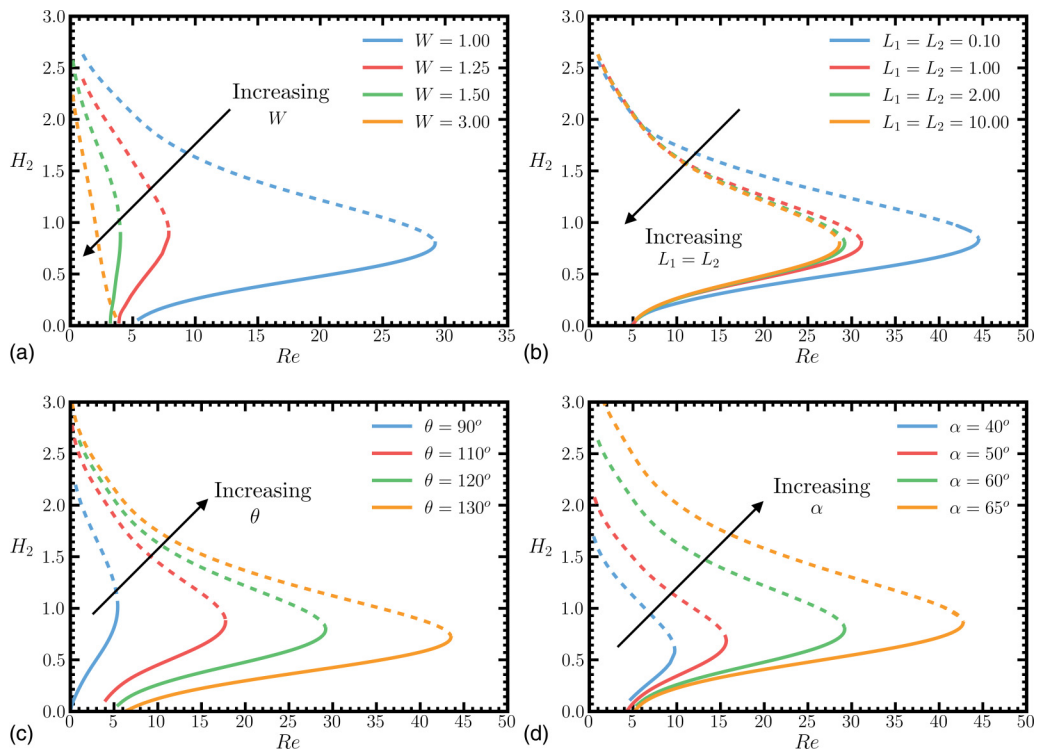


FIG. 13. Wetting length H_2 as a function of Re for different (a) slit-widths, W , for $L_1 = L_2 = 2$, (b) inflow and outflow lengths of the unit cell for $W = 1$ and $Ka = 10$, $\alpha = 60^\circ$, and $\theta = 120^\circ$, (c) substrate wettabilities for $W = 1$, $L_1 = L_2 = 2$, $Ka = 10$, and $\alpha = 60^\circ$, and (d) inclination angles for $W = 1$, $L_1 = L_2 = 2$, $Ka = 10$, and $\theta = 120^\circ$.

arises. Regarding the lower solution branch, the wetting distance H_2 obtains significantly smaller values corresponding to very shallow penetration inside the slit. As shown in Fig. 12(c), the film overpasses the slit with small deformation of the inner interface. Increasing the Reynolds number in the lower branch, the contact line moves deeper inside the slit up to the turning point (i.e., for $Ka = 10$ at $Re \sim 29$). As will be discussed in the following section, the stability characteristics of these two solution branches are quite different, and in fact, it will be demonstrated that the upper solution branch is always unstable. In contrast, the lower solution branch can be stable under conditions and therefore it is the only one that could be observed in a physical setup.

With increasing values of Ka steady solutions are found to exist up to higher values of Re since, as shown in Fig. 12(a), the turning point arises for $Re = 17.11, 29.16, 35.35, 37.95$ for $Ka = 5, 10, 12.5, 15$, respectively. One way to understand the strong dependency of the location of the turning point on liquid properties is by considering the fact that under a constant value of flowrate but with increasing viscosity (i.e., decreasing Ka), capillary forces become weaker, not able to counteract gravity pushing liquid deep inside the cavity, and thus the wetting distance increases. Therefore, the turning point arises at lower values of the Reynolds number for decreasing values of Ka . It is noteworthy, though, that the wetting distance which arises for the maximum value of Re (i.e., at the turning point) is relatively constant ($H_{2,\max} \sim 0.78$) and does not depend on the liquid properties.

In Fig. 13 we present a parametric study to briefly examine the effects of the geometrical characteristics and wetting properties of the substrate on the steady flow as well as the effect of the inclination angle. We will focus our discussion mainly on the lower solution branch since this

solution is physically of greater importance. As shown in Fig. 13(a), with decreasing the width of the slit, the increased effect of the capillary forces at the inner interface (the capillary force is proportional to σ^*/W^*) prevents the film from intruding deep inside the topographical feature. Therefore, the detachment takes place for significantly higher values of the flowrate (i.e., H_2 acquires positive values for higher values of Re). Specifically, we note that for a narrow slit with $W = 1$ and $Tr = 4$, the solution is bounded in the range $4.90 < Re < 29.90$. However, for slits with larger widths, the supporting effect of the capillary force weakens, and the range of Re for which a stable solution is possible decreases considerably, e.g., see for $W = 1.25$ and 1.50 . There is a certain value of W , where the stable branch vanishes and the entire steady solution becomes unstable; e.g., see the case for $W = 3$. As a result, partial wetting of this type cannot be observed in cases where the dimensional width of the slit is larger than $3l_c^*$.

In Fig. 13(b) we examine the effect of inflow and outflow lengths of the periodic unit cell while keeping the width constant, thereby varying the relative size of the slit and the flat part of the substrate. In this figure, we present the wetting distance H_2 as a function of Re for $L_1 = L_2 = 10, 2, 1, 0.1$. For substrates with a long entrance region, the solution tends to the asymptotic limit of an isolated slit, e.g., see solutions for $L_1 = L_2 = 10, 2$. Decreasing the length of the entrance region, the substrate tends to a pillar-like structure. The reduced effect of the shear stresses experienced by the liquid, since most of the liquid remains suspended in the air, results in increased film velocity with a considerably thinner profile (for a similar flow rate), inhibiting wetting of the downstream wall. Therefore, the stable branch of the steady-state solution is extended to a higher range of Re for the film to reach the maximum sustainable wetting length. The maximum value of the Reynolds number was calculated to be $Re = 31.10$ and 44.55 for $L_1 = L_2 = 1$ and 0.1 , respectively.

In Fig. 13(c) we examine the effect of the substrate wettability, θ , on the wetting length of the upstream wall, by keeping the liquid properties fixed and the inclination angle at $\alpha = 60^\circ$. The more hydrophobic the substrate is, the larger the magnitude of the force applied on the contact point, since $F_{CL}^* \sim \sigma^* \cos \theta$. Thus, the flowrate should obtain higher values in order for gravity to balance the effect of capillary forces. Indeed, in Fig. 13(c) we observe that as the substrate becomes more hydrophobic, the flow curves are extended to higher values of Re . Also, the wetting distance at the turning point is affected by the equilibrium contact angle, since H_2 was calculated to be $1.00, 0.87, 0.80, 0.72$ for $\theta = 90^\circ, 110^\circ, 120^\circ, \text{ and } 130^\circ$, respectively. The latter can be attributed to the fact that the higher wettability of the substrate favors deeper penetration of the contact line. For the completeness of the parametric study, we also present in Fig. 13(d) the effect of the orientation of the substrate with respect to gravity. By decreasing the inclination angle, the y component of the gravity force becomes more efficient to push the liquid inside the slit, leading to deeper penetration for the same flow rate. The decreased penetration for higher inclination angles, on the other hand, leads to higher maximum values of Re that can sustain a steady flow.

b. Linear stability analysis

Next, we turn our attention to the stability of the steady solutions presented above when subjected to disturbances of arbitrary wavelengths. To identify the stability of the two solution branches, we present in Fig. 14 the eigenspectra for two steady states that lie at the upper and lower branch for $Ka = 10$, $\alpha = 60^\circ$ and $\theta = 120^\circ$ and for $Re = 5$ and 5.8 , considering values of the Bloch wave number Q in the range $[0,1)$; spectra shown in Figs. 14(a) and 14(c) correspond to steady solutions similar to those depicted in Figs. 12(b) and 12(c), respectively. As shown in Fig. 14(a), for $Re = 5.8$ many calculated eigenvalues have a positive real part denoting that the steady solution of the upper branch is highly unstable. The most critical eigenvalue has zero imaginary part ($\lambda = 0.13 + 0i$), denoting that the steady solution is unstable due to a “nonoscillatory” eigenmode. Moreover, since the most dangerous eigenvalue arises for $Q = 0$, the corresponding mode of instability has the same periodicity with the unit cell; the latter is true for all steady solutions with higher values of Re that are part of the upper branch. Increasing Re and moving along the upper solution branch, the

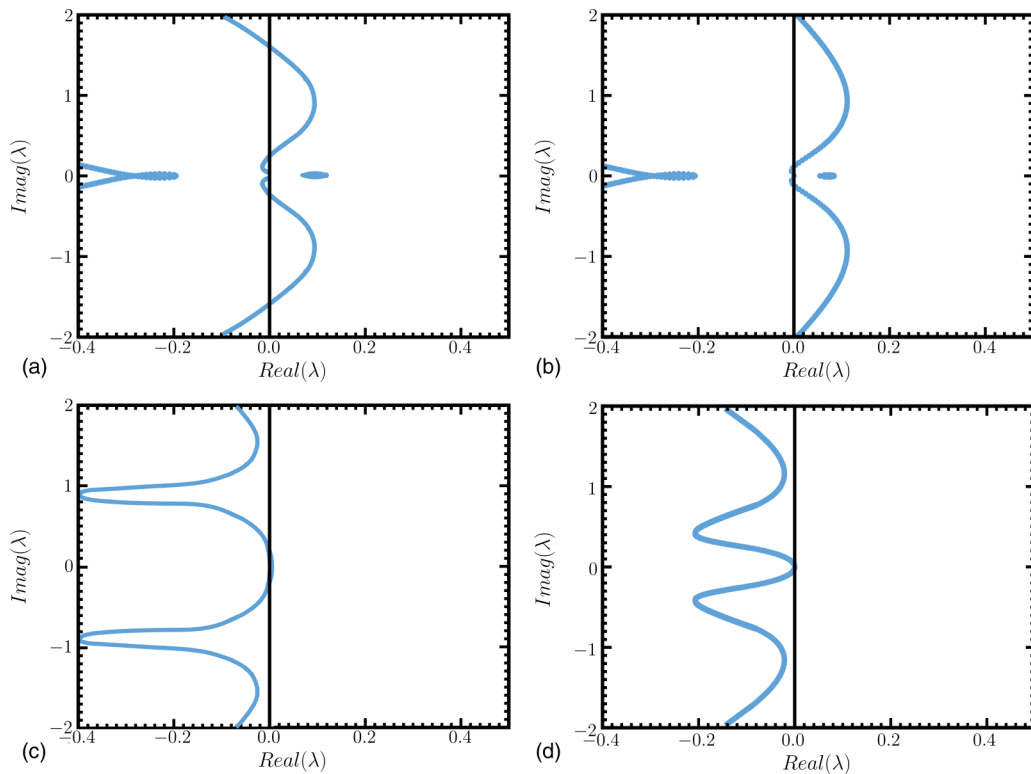


FIG. 14. Eigenspectra for $Q \in [0, 1)$ corresponding to the steady states shown in Fig. 12 for $Ka = 10$. Panels (a) and (b) depict the spectrum that corresponds to the upper solution branch for $Re = 5.8$ and 5.0 , respectively. Panels (c) and (d) depict the spectrum that corresponds to the lower solution branch for $Re = 5.8$ and 5.0 , respectively.

most dangerous eigenvalue acquires real part with decreasing magnitude and eventually, marginal stability is obtained at $Re = 29.77$, i.e., the location of the turning point in Fig. 12(a) for $Ka = 10$. Regarding the stability of the steady solutions of the upper branch for lower values of Re [e.g., see Fig. 14(b) for $Re = 5$], the flow is unstable, and the most dangerous eigenvalues acquire a nonzero imaginary part indicating the appearance of an oscillatory type of instability. Turning our attention to the stability of the lower branch solution [see Figs. 14(c) and 14(d)], we find that the flow is stable for all values of Q , since both the isolated eigenvalues and the continuum part of the spectrum have a negative real part. Therefore, we can deduce that out of all possible configurations for partial wetting of the sidewalls of the substrate, the steady solutions lie in the lower branch [see Fig. 12(a) and Fig. 14; i.e., a film with restricted partially wetting of the downstream wall and completely dewetted ($H_1 = 0$) upstream sidewall] are the only ones that can be conditionally stable. Hereafter, we will focus our study solely on this flow configuration and examine in detail its linear stability to determine the critical conditions for instability.

To this end, we produce stability maps presented in the (Re, f) plane to investigate critical conditions when such steady flow configurations are subjected to disturbances of arbitrary wavelength and frequency. In Fig. 15(a) we depict the stability maps for three different values of $Ka = 5, 10, 12.5$ with colored areas corresponding to unstable configurations, whereas white areas denote regimes where the flow is stable. In general, the increase of Ka tends to stabilize the fluid flow both under long-wave and finite wavelength disturbances. For some values of Ka , we observe that the flow is most unstable at disturbances with finite frequency ($f \neq 0$); for instance, for $Ka = 5$ the most critical disturbance arises for $f = 0.08$ at $Re_c = 2.96$. We note that this behavior differs from

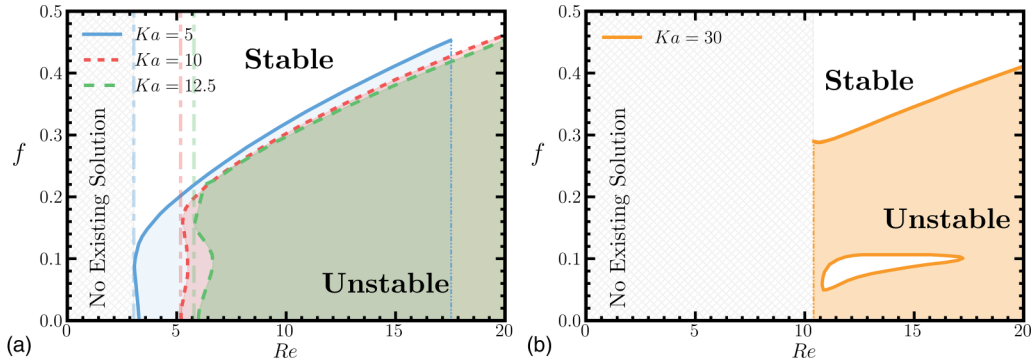


FIG. 15. Stability diagrams for different values of Ka for $L_1 = L_2 = 2$, $W = 1$, $\alpha = 60^\circ$, and $\theta = 120^\circ$.

the ideal Cassie-Baxter state, in which the most unstable mode was encountered for long-wave disturbances ($f \rightarrow 0$). This effect can be attributed to the presence of the moving contact line at the downstream wall, which provides an additional mechanism that dampens low-frequency oscillations (a more detailed discussion of this mechanism is given below). Additionally, in Fig. 15(a) we observe that the neutral curves are terminated abruptly, and the corresponding limits of the steady state are depicted in the stability maps as dashed lines in the figure. This is because, as noted above, the steady-state solution is possible only for a short range of flow rates; steady solutions cease to exist beyond the turning point; see Fig. 12(a). For high values of Ka , e.g., see the case for $Ka = 30$, the flow is unconditionally unstable when subjected to long-wave disturbances [see Fig. 15(b)]; the dashed line denotes that no steady solutions can be found for Re below that limit [see also Fig. 12(a)]. The flow, in this case, is found to be stable only at high-frequency disturbances (i.e., $f > 0.29$) or to disturbances that correspond to the regime of the stable isle that is shown in Fig. 15(b); the presence of this isle of stability could be attributed to the interaction of the two interfaces that provide as discussed above a mechanism for the stabilization of the flow.

To examine the effect of the geometrical characteristics of the substrate, we depict in Fig. 16(a) the stability diagrams for three different inflow and outflow lengths of the unit cell, $L_1 = L_2 = 0.1, 1, 2$ while keeping constant the slit width, $W = 1$. We find that the neutral curves are shifted to higher values of Re , and therefore, the flow becomes stabilized as the geometry of the substrate tends to a pillar-like structure, with decreasing inflow and outflow lengths of the unit cell; for $L_1 = L_2 = 0.1$ the flow becomes most unstable when subjected to disturbances with $f = 0.22$ and critical conditions arise at $Re_c = 7.36$. Increasing the width of the solid parts of the substrate (i.e., increase

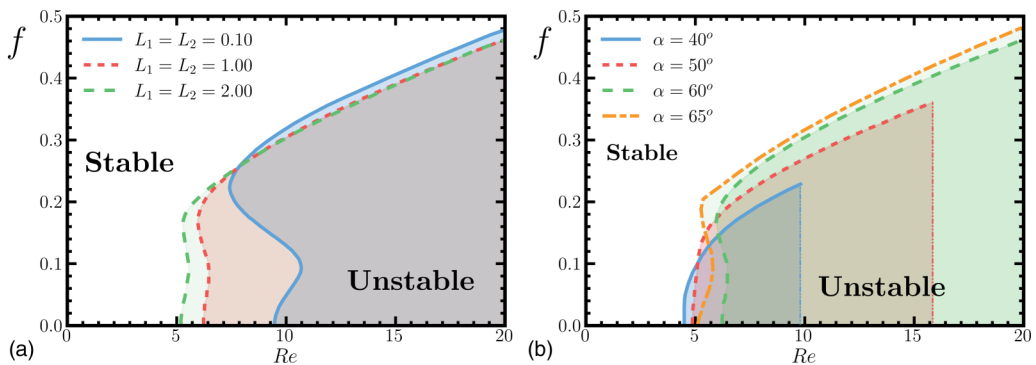


FIG. 16. Stability diagrams for different (a) inflow and outflow lengths of the unit cell and $\alpha = 60^\circ$ and (b) inclination angles and for $L_1 = L_2 = 2$. The remaining parameter values are $Ka = 10$, $W = 1$, and $\theta = 120^\circ$.

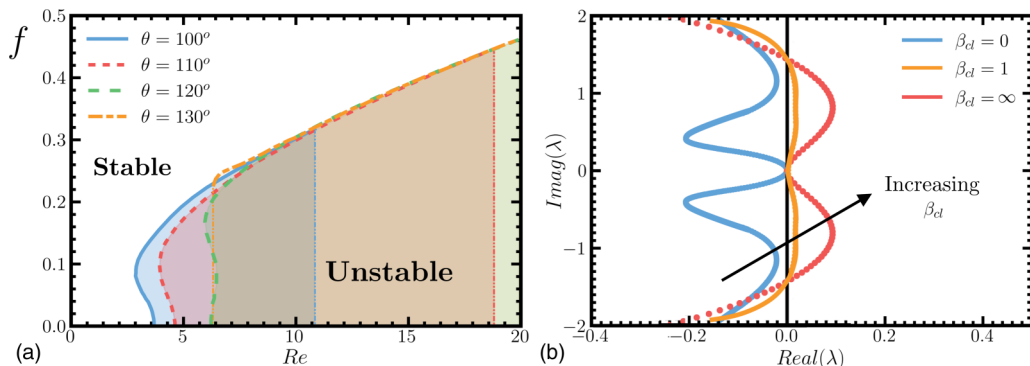


FIG. 17. (a) Stability diagrams for substrates with different wettability. (b) Eigenspectrum for different values of β_{cl} , $Re = 5$. The remaining parameter values are $Ka = 10$, $W = 1$, $\alpha = 60^\circ$, and $\theta = 120^\circ$.

of L_1 and L_2) causes the destabilization of the flow approaching the critical conditions of Nusselt flat film flow, as the stabilizing role of the inner interface becomes increasingly less important. Finally, in Fig. 16(b), we examine the impact of the inclination angle of the substrate on the stability of the flow, i.e., for $\alpha = 40^\circ, 50^\circ, 60^\circ, 65^\circ$. Interestingly, the critical conditions for the onset of instability are relatively constant, since it was calculated to be $Re_c = 4.39, 4.77, 5.09$ for $\alpha = 40^\circ, 50^\circ, 60^\circ$, respectively. It is noteworthy that for $\alpha = 60^\circ$ and 65° the stability maps indicate that the most critical value of Re arises under finite frequency disturbances, depicting the stabilization of the flow, especially for long-wave disturbances.

To conclude our parametric study, we also examine the effect of substrate wettability on the stability of the flowing film. To this end, we present in Fig. 17(a) neutral curves for different values of the equilibrium contact angle $\theta = 100^\circ, 110^\circ, 120^\circ, 130^\circ$. We have already seen in Fig. 13(c) that with increasing hydrophobicity of the substrate, steady solutions can be achieved for a wider range of Re . This is also reflected in Fig. 17(a) (the dashed line indicates the maximum value of Re for which a steady solution exists). Regarding the flow stability, it is clearly shown in this figure that for low contact angles, the flow is most unstable for high-frequency disturbances. With increasing hydrophobicity of the substrate (e.g., for $100^\circ \leq \theta \leq 120^\circ$) the critical Re for instability increases and the flow becomes stabilized. On the other hand, for large values of the contact angle ($\theta \geq 130^\circ$) the flow tends to the ideal Cassie-Baxter limit with no wetting of the downstream wall for low values of Re [see Fig. 13(c)], and steady solutions are possible only for $Re \geq 6.32$. Nevertheless, as can be seen in Fig. 17(a), the flow is found to be unstable for low-frequency disturbances.

One last question that needs to be addressed is about the effect of the contact line mobility along the slit sidewalls on the stability of the flow. So far, we have considered the case of $\beta_{cl} = 0$ and therefore, we have assumed that the contact line is able to move freely to obtain the equilibrium contact angle instantaneously; the effect of β_{cl} can be seen in Eq. (13). This scenario would be expected in the case of an ideally smooth substrate. However, it is interesting to examine the effect of a less mobile contact line or even in the limiting case where the contact line remains pinned, e.g., due to a defect at the surface of the substrate. To account for these cases, we have examined in Fig. 17(b) the eigenspectrum for three different values of β_{cl} . We consider the cases of (1) $\beta_{cl} = 0$ for which the contact line instantaneously forms the equilibrium contact angle, (2) $\beta_{cl} \rightarrow \infty$ for which the contact line remains pinned, and (3) $\beta_{cl} = 1$ to simulate a case with restricted mobility of the contact line. Interestingly, we find that for $\beta_{cl} = 0$ all the eigenvalues have a negative real part which indicates that this configuration is the most stable, while for $\beta_{cl} \rightarrow \infty$ a significant part of the spectrum lies in the regime with positive real parts indicating that the flow, in this case, is highly unstable. As expected for intermediate values of β_{cl} the eigenspectra progressively transit from one state to the other. Therefore, it is shown that the ability of the contact line to move provides an additional mechanism for the stabilization of the flow, acting as a damper for the flow disturbances.

Moreover, this result also indicates that the microroughness of the substrate and the possible effects of contact angle hysteresis could also have an important impact on the flow stability.

V. CONCLUSIONS

This work presents a theoretical analysis of the hydrodynamics and stability of a film flowing over a substrate featuring a periodic array of deep slits. Due to the small scale of these slits, the film partially wets the solid substrate encapsulating air inside the solid structures and thus forming a second gas-liquid interface. We numerically solve the governing equations employing the finite element method and explore the possibility of multiple steady states that may arise because of a second free surface in the system and the presence of two contact lines along the slit sidewalls. Through detailed parametric analysis, we elucidate the effect of the geometrical, wetting, and flow parameters on the possible steady configurations of the liquid film and their effect on the deformation of both liquid-gas interfaces and degree of wetting of the substrate grooves. Additionally, we perform a linear stability analysis to identify which of these possible steady configurations can be encountered in an experimental setup by examining the stability of the steady solution when subjected to infinitesimal 2D disturbances in the streamwise direction. Through this analysis, it is also possible to identify the various stabilization/destabilization mechanisms which can affect the dynamic response of this system. To the best of our knowledge, this is the first linear stability analysis of a film flowing over partially wetted microstructured substrates.

We first examine the case of a film-forming an ideal Cassie-Baxter state, where the inner liquid-air interface does not wet the slit sidewalls with the contact lines pinned at their edges and demonstrate that the steady-state configuration of the flow of low viscosity liquids is highly affected by the presence of the second gas interface due to the presence of a shear-free region arising at the midplane of the slits; the latter significantly affects the apparent slip of the liquid at the level of the solid substrate, providing a noticeable drag reduction, in agreement with previous reports [20,26,27]. Interestingly, our linear stability analysis also revealed that the second gas-liquid interface has a nontrivial role in the overall stability of the system. It is shown that the inner liquid-gas interface significantly affects the critical conditions, delaying the transition to instability. The flexibility of the inner free surface may provide an additional stabilization mechanism acting as a damper for the disturbances, which mainly develop along with the external liquid-gas interface. However, in low-viscosity liquids, the flow may actually be destabilized due to the decrease of the macroscopic drag coefficient which renders the destabilizing effect of inertia increasingly important.

In the second half of the paper, we focused on the examination of partially wetted states which typically arise for slit widths larger than the capillary length of the liquid. It is shown that, under the same flow conditions, four different steady states arise, which have been analyzed for their stability. Interestingly, we find that out of these four possible configurations, three are unconditionally unstable. The only steady configuration which is conditionally stable arises for the case where the liquid partially wets only the downstream wall with complete dewetting of the upstream wall; such a configuration was found to be possible for a short range of slit widths ($l_c^* < W^* < 3l_c^*$). The examination of the stability of the latter configuration reveals that the mobility of the contact line along the upstream wall provides an additional stabilization mechanism, apart from the regular stabilization mechanism of the flexible inner interface.

Our findings clearly indicate that the flow dynamics can be very interesting, with important implications for flows over superhydrophobic surfaces, and therefore this work should be complemented in the future with detailed experimental studies. To the best of our knowledge, such studies are lacking, despite the vast experimental work that exists on the stability of falling films for fully wetted substrates. Moreover, the present work focused on the flow over deep structures. Partial wetting can also be achieved, though, even for cases that the structures are not so deep. As shown in the works of [32,35–37], the liquid may assume other configurations in between the two extremes of complete wetting (Wenzel state) or no wetting the trench floor (examined herein). The study of the stability characteristics of the latter configurations is already under way.

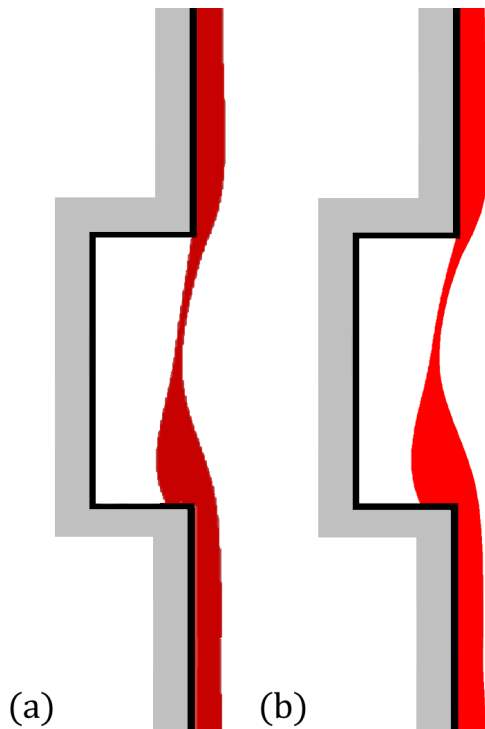


FIG. 18. Comparison of (a) the simulation in OpenFoam by Lampropoulos *et al.* [36], with (b) the predictions of our in-house FEM code, for $Re = 6 \times 10^{-4}$, $Ka = 13.9 \times 10^{-2}$, $a = 89.50^\circ$, $\theta = 120^\circ$, $L_1 = L_2 = 10$, and $W = 2.79$.

ACKNOWLEDGMENTS

This work has been supported by the LIMMAT foundation under the grant MuSiComPS and the Hellenic Foundation of Research and Innovation under the grant HFRI FM17-2309 MOFLOWMAT. G.K. would like to acknowledge the financial support from the Hellenic Foundation for Research and Innovation (HFRI) and the General Secretariat for Research and Technology (GSRT), under Grant Agreement No. 792.

APPENDIX: CODE VALIDATION

This appendix presents the validation of our in-house FEM code by comparing its predictions against other works in the literature.

1. Base state

First, we compare our steady-state calculations against the predictions provided by Lampropoulos *et al.* [36]. These authors performed transient simulations of gravity-driven Newtonian films over substrates with rectangular topographical features, using the volume of fluid (VOF) method implemented in the OpenFoam software package. For $Re = 6 \times 10^{-4}$, $Ka = 13.9 \times 10^{-2}$, $a = 89.50^\circ$, $\theta = 120^\circ$, $L_1 = L_2 = 10$, and $W = 2.79$ it was shown by Lampropoulos *et al.* [36] that the film partially wets the substrate and Fig. 18(a) depicts the resulting steady configuration (achieved at $t = 126.4$). The results of our work for the same values of the dimensionless groups [shown in Fig. 18(b)] are in excellent agreement with the predictions of Lampropoulos *et al.* [36] in terms of both the steady shape of interfaces as well as the wetting distances along the sidewalls.

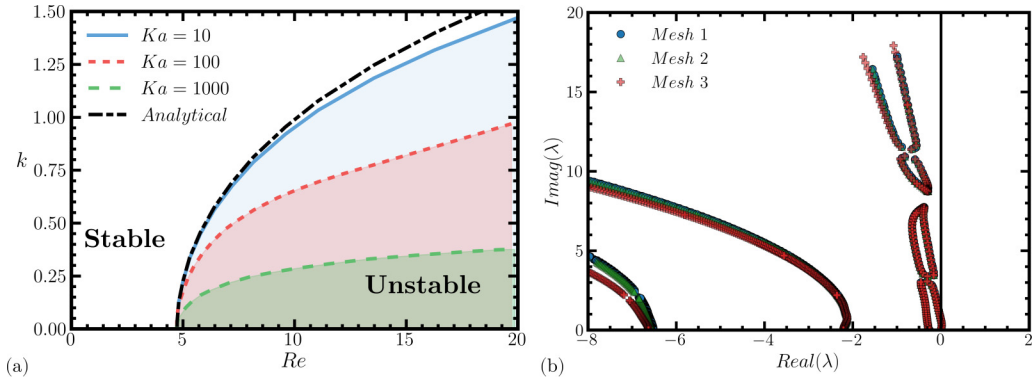


FIG. 19. (a) Stability maps for Nusselt flow. The solid lines depict the predictions of our in-house FEM code, and the black dashed line depicts the predictions from the analytical expression (A1) for $Ka = 10$. (b) Mesh convergence test for the computed eigenspectrum of the ideal Cassie-Baxter state and for $Re = 10$, $Ka = 100$, $L = 1$, and $Tr = 0.67$. The mesh properties can be found in Table II.

2. Linear stability

In Fig. 19(a) we present the validation for the stability predictions of our code considering two limiting cases related to our configuration of a partially wetted substrate. In particular, Fig. 19(a) depicts the predicted stability maps for the limiting case of a liquid falling film flowing over a flat solid substrate. As shown for $L = 10$, $a = 10^\circ$ and for three different values of the Kapitza number, our predictions for the critical Reynolds number, Re_c , are in very good agreement with the following analytical expression for the onset of instability (as predicted by the works of Benjamin [38] and Yih [39]):

$$Re_c = \frac{5}{6} \cot(a) + \frac{5}{6} k^2 Ka \left(\frac{1}{\sin \alpha (3Re_c)^2} \right)^{1/3}. \quad (A1)$$

In the above expression, k denotes the wave number of the corresponding disturbance. The small deviation from the analytical expression for large values of k can be attributed to the fact that (A1) was obtained using the long-wave approximation rendering it valid only for low values of k ; this effect has also been noted by Trifonov [44].

Regarding the flow of a film over substrate with slits, we performed a mesh convergence for the computed eigenspectrum for the ideal Cassie-Baxter state, where the inner liquid-air interface does not wet the slit sidewalls and the contact lines remain pinned at their edges. In contrast to other common flows, such as those encountered in the extrusion processes [53,64], in film flows, instabilities are characterized by low frequencies, and hence they exhibit fast convergence with mesh refinement. In Fig. 19(b) we present the most dangerous part of the eigenspectrum calculated for three distinct meshes, see Table II and for $Re = 10$ and $Ka = 100$, $L = 1$, and $Tr = 0.67$. As is evident, all the eigenvalues converge nicely as the mesh discretization increases, especially the most critical eigenvalues (those with the largest real part).

TABLE II. Table with the properties of the meshes used for the mesh convergence.

Mesh	No. of elements in x direction	No. of elements in y direction	Total no. of triangular elements
Mesh 1	150	10	3000
Mesh 2	75	10	1500
Mesh 3	30	10	600

-
- [1] R. V. Craster and O. K. Matar, Dynamics and stability of thin liquid films, *Rev. Mod. Phys.* **81**, 1131 (2009).
- [2] L. E. Stillwagon and R. G. Larson, Leveling of thin films over uneven substrates during spin coating, *Phys. Fluids A* **2**, 1937 (1990).
- [3] N. Miljkovic, R. Enright, and E. N. Wang, Effect of droplet morphology on growth dynamics and heat transfer during condensation on superhydrophobic nanostructured surfaces, *ACS Nano* **6**, 1776 (2012).
- [4] R. Blossey, Self-cleaning surfaces—Virtual realities, *Nature Mater.* **2**, 301 (2003).
- [5] Y. Liu, L. Moevius, X. Xu, T. Qian, J. M. Yeomans, and Z. Wang, Pancake bouncing on superhydrophobic surfaces, *Nat. Phys.* **10**, 515 (2014).
- [6] L. Cao, A. K. Jones, V. K. Sikka, J. Wu, and D. Gao, Anti-icing superhydrophobic coatings, *Langmuir* **25**, 12444 (2009).
- [7] D. Quéré, Wetting and roughness, *Annu. Rev. Mater. Res.* **38**, 71 (2008).
- [8] J. P. Rothstein, Slip on superhydrophobic surfaces, *Annu. Rev. Fluid Mech.* **42**, 89 (2010).
- [9] D. Gropper, L. Wang, and T. J. Harvey, Hydrodynamic lubrication of textured surfaces: A review of modeling techniques and key findings, *Tribol. Int.* **94**, 509 (2016).
- [10] B. Dean and B. Bhushan, Shark-skin surfaces for fluid-drag reduction in turbulent flow: A review, *Phil. Trans. R. Soc. A* **368**, 4775 (2010).
- [11] R. N. Wenzel, Resistance of solid surfaces to wetting by water, *Ind. Eng. Chem.* **28**, 988 (1936).
- [12] S. Kalliadasis and G. M. Homsy, Stability of free-surface thin-film flows over topography, *J. Fluid Mech.* **448**, 387 (2001).
- [13] S. Kalliadasis, C. Bielarz, and G. M. Homsy, Steady free-surface thin film flows over topography, *Phys. Fluids* **12**, 1889 (2000).
- [14] P. H. Gaskell, P. K. Jimack, M. Sellier, H. M. Thompson, and M. C. T. Wilson, Gravity-driven flow of continuous thin liquid films on non-porous substrates with topography, *J. Fluid Mech.* **509**, 253 (2004).
- [15] A. Wierschem, V. Bontozoglou, C. Heining, H. Uecker, and N. Aksel, Linear resonance in viscous films on inclined wavy planes, *Int. J. Multiphase Flow* **34**, 580 (2008).
- [16] P.-K. Nguyen and V. Bontozoglou, Steady solutions of inertial film flow along strongly undulated substrates, *Phys. Fluids* **23**, 052103 (2011).
- [17] A. B. D. Cassie and S. Baxter, Wettability of porous surfaces, *Trans. Faraday Soc.* **40**, 546 (1944).
- [18] J. R. Philip, Flows satisfying mixed no-slip and no-shear conditions, *Zs Angew. Math. Phys.* **23**, 353 (1972).
- [19] J. R. Philip, Integral properties of flows satisfying mixed no-slip and no-shear conditions, *J. Appl. Math. Phys.* **23**, 960 (1972).
- [20] J. Ou and J. P. Rothstein, Direct velocity measurements of the flow past drag-reducing ultrahydrophobic surfaces, *Phys. Fluids* **17**, 103606 (2005).
- [21] P. Tsai, A. M. Peters, C. Pirat, M. Wessling, R. G. H. Lammertink, and D. Lohse, Quantifying effective slip length over micropatterned hydrophobic surfaces, *Phys. Fluids* **21**, 112002 (2009).
- [22] D. Maynes, K. Jeffs, B. Woolford, and B. W. Webb, Laminar flow in a microchannel with hydrophobic surface patterned microribs oriented parallel to the flow direction, *Phys. Fluids* **19**, 093603 (2007).
- [23] D. Crowdy, Slip length for longitudinal shear flow over a dilute periodic mattress of protruding bubbles, *Phys. Fluids* **22**, 121703 (2010).
- [24] D. G. Crowdy, Analytical formulae for longitudinal slip lengths over unidirectional superhydrophobic surfaces with curved menisci, *J. Fluid Mech.* **791**, R7 (2016).
- [25] S. E. Game, M. Hodes, E. E. Keaveny, and D. T. Papageorgiou, Physical mechanisms relevant to flow resistance in textured microchannels, *Phys. Rev. Fluids* **2**, 094102 (2017).
- [26] S. E. Game, M. Hodes, and D. T. Papageorgiou, Effects of slowly varying meniscus curvature on internal flows in the Cassie state, *J. Fluid Mech.* **872**, 272 (2019).
- [27] C. Lee, C.-H. Choi, and C.-J. Kim, Superhydrophobic drag reduction in laminar flows: A critical review, *Exp. Fluids* **57**, 176 (2016).
- [28] D. Song, B. Song, H. Hu, X. Du, P. Du, C.-H. Choi, and J. P. Rothstein, Effect of a surface tension gradient on the slip flow along a superhydrophobic air-water interface, *Phys. Rev. Fluids* **3**, 033303 (2018).

- [29] P. Dey, S. K. Saha, and S. Chakraborty, Confluence of channel dimensions and groove width dictates slippery hydrodynamics in grooved hydrophobic confinements, *Microfluid. Nanofluid.* **24**, 23 (2020).
- [30] E. Lisi, M. Amabili, S. Meloni, A. Giacomello, and C. M. Casciola, Self-recovery superhydrophobic surfaces: Modular design, *ACS Nano* **12**, 359 (2018).
- [31] S. Huang, P. Lv, and H. Duan, Morphology evolution of liquid–gas interface on submerged solid structured surfaces, *Extreme Mech. Lett.* **27**, 34 (2019).
- [32] A. Giacomello, M. Chinappi, S. Meloni, and C. M. Casciola, Metastable Wetting on Superhydrophobic Surfaces: Continuum and Atomistic Views of the Cassie-Baxter–Wenzel Transition, *Phys. Rev. Lett.* **109**, 226102 (2012).
- [33] G. Karapetsas, N. T. Chamakos, and A. G. Papanthanasidou, Efficient modelling of droplet dynamics on complex surfaces, *J. Phys. Condens. Matter* **28**, 085101 (2016).
- [34] D. Pettas, G. Karapetsas, Y. Dimakopoulos, and J. Tsamopoulos, On the degree of wetting of a slit by a liquid film flowing along an inclined plane, *J. Fluid Mech.* **820**, 5 (2017).
- [35] S. Varchanis, Y. Dimakopoulos, and J. Tsamopoulos, Steady film flow over a substrate with rectangular trenches forming air inclusions, *Phys. Rev. Fluids* **2**, 124001 (2017).
- [36] N. K. Lampropoulos, Y. Dimakopoulos, and J. Tsamopoulos, Transient flow of gravity-driven viscous films over substrates with rectangular topographical features, *Microfluid. Nanofluid.* **20**, 51 (2016).
- [37] G. Karapetsas, N. K. Lampropoulos, Y. Dimakopoulos, and J. Tsamopoulos, Transient flow of gravity-driven viscous films over 3D patterned substrates: Conditions leading to Wenzel, Cassie and intermediate states, *Microfluid. Nanofluid.* **21**, 17 (2017).
- [38] T. B. Benjamin, Wave formation in laminar flow down an inclined plane, *J. Fluid Mech.* **2**, 554 (1957).
- [39] C.-S. Yih, Stability of liquid flow down an inclined plane, *Phys. Fluids* **6**, 321 (1963).
- [40] M. Vlachogiannis and V. Bontozoglou, Experiments on laminar film flow along a periodic wall, *J. Fluid Mech.* **457**, 133 (2002).
- [41] T. Pollak and N. Aksel, Crucial flow stabilization and multiple instability branches of gravity-driven films over topography, *Phys. Fluids* **25**, 024103 (2013).
- [42] D. Pettas, G. Karapetsas, Y. Dimakopoulos, and J. Tsamopoulos, Viscoelastic film flows over an inclined substrate with sinusoidal topography, II. Linear stability analysis, *Phys. Rev. Fluids* **4**, 083304 (2019).
- [43] D. Pettas, G. Karapetsas, Y. Dimakopoulos, and J. Tsamopoulos, Viscoelastic film flows over an inclined substrate with sinusoidal topography. I. Steady state, *Phys. Rev. Fluids* **4**, 083303 (2019).
- [44] Y. Trifonov, Stability of a film flowing down an inclined corrugated plate: The direct Navier-Stokes computations and Floquet theory, *Phys. Fluids* **26**, 114101 (2014).
- [45] G. Karapetsas and V. Bontozoglou, The primary instability of falling films in the presence of soluble surfactants, *J. Fluid Mech.* **729**, 123 (2013).
- [46] G. Karapetsas and V. Bontozoglou, The role of surfactants on the mechanism of the long-wave instability in liquid film flows, *J. Fluid Mech.* **741**, 139 (2014).
- [47] J. P. Alexander, T. L. Kirk, and D. T. Papageorgiou, Stability of falling liquid films on flexible substrates, *J. Fluid Mech.* **900**, A40 (2020).
- [48] A. Sharma, P. K. Ray, and D. T. Papageorgiou, Dynamics of gravity-driven viscoelastic films on wavy walls, *Phys. Rev. Fluids* **4**, 063305 (2019).
- [49] A. Samanta, C. Ruyer-Quil, and B. Goyeau, A falling film down a slippery inclined plane, *J. Fluid Mech.* **684**, 353 (2011).
- [50] D. Bonn, J. Eggers, J. Indekeu, J. Meunier, and E. Rolley, Wetting and spreading, *Rev. Mod. Phys.* **81**, 739 (2009).
- [51] M. Pavlidis, Y. Dimakopoulos, and J. Tsamopoulos, Steady viscoelastic film flow over 2D topography: I. The effect of viscoelastic properties under creeping flow, *J. Non-Newtonian Fluid Mech.* **165**, 576 (2010).
- [52] M. Pavlidis, G. Karapetsas, Y. Dimakopoulos, and J. Tsamopoulos, Steady viscoelastic film flow over 2D Topography: II. The effect of capillarity, inertia and substrate geometry, *J. Non-Newtonian Fluid Mech.* **234**, 201 (2016).
- [53] D. Pettas, G. Karapetsas, Y. Dimakopoulos, and J. Tsamopoulos, On the origin of extrusion instabilities: Linear stability analysis of the viscoelastic die swell, *J. Non-Newtonian Fluid Mech.* **224**, 61 (2015).

- [54] Y. Dimakopoulos and J. Tsamopoulos, A quasi-elliptic transformation for moving boundary problems with large anisotropic deformations, *J. Comput. Phys.* **192**, 494 (2003).
- [55] N. Chatzidai, A. Giannousakis, Y. Dimakopoulos, and J. Tsamopoulos, On the elliptic mesh generation in domains containing multiple inclusions and undergoing large deformations, *J. Comput. Phys.* **228**, 1980 (2009).
- [56] M. A. Spaid and G. M. Homsy, Stability of Newtonian and viscoelastic dynamic contact lines, *Phys. Fluids* **8**, 460 (1996).
- [57] H. J. Pain, *The Physics of Vibrations and Waves*, 6th ed. (Wiley, Chichester, 2008).
- [58] K. N. Christodoulou, *Computational Physics of Slide Coating Flow*, Volumes I and II, Ph.D. Thesis, University of Minnesota, 1990.
- [59] G. Karapetsas and J. Tsamopoulos, On the stick-slip flow from slit and cylindrical dies of a Phan-Thien and Tanner fluid model. II. Linear stability analysis, *Phys. Fluids* **25**, 093105 (2013).
- [60] R. Natarajan, An Arnoldi-based iterative scheme for nonsymmetric matrix pencils arising in finite element stability problems, *J. Comput. Phys.* **100**, 128 (1992).
- [61] R. B. Lehoucq, D. C. Sorensen, and C. Yang, Arpack: Solution of large scale eigenvalue problems with implicitly restarted Arnoldi methods. User's guide. www.caam.rice.edu/software/arpack (1997).
- [62] S. J. D. D'Alessio, J. P. Pascal, and H. A. Jasmine, Instability in gravity-driven flow over uneven surfaces, *Phys. Fluids* **21**, 062105 (2009).
- [63] D. Tseluiko, M. G. Blyth, and D. T. Papageorgiou, Stability of film flow over inclined topography based on a long-wave nonlinear model, *J. Fluid Mech.* **729**, 638 (2013).
- [64] S. Varchanis, D. Pettas, Y. Dimakopoulos, and J. Tsamopoulos, Origin of the Sharkskin Instability: Nonlinear Dynamics, *Phys. Rev. Lett.* **127**, 088001 (2021).